

1 Direct Comparison of Numerical Simulations 2 and Experiments of CO₂ Injection and 3 Migration in Geologic Media: Value of Local 4 Data and Forecasting Capability

5 Lluís Saló-Salgado^{1,2}, Malin Haugen³, Kristoffer
 6 Eikehaug³, Martin Fernø^{3,4*}, Jan M. Nordbotten^{5,4*}
 7 and Ruben Juanes^{1,2*}

8 ¹*Department of Civil and Environmental Engineering,
 9 Massachusetts Institute of Technology, Cambridge, 02139, MA,
 10 USA.

11 ²Earth Resources Laboratory, Department of Earth, Atmospheric
 12 and Planetary Sciences, Massachusetts Institute of Technology,
 13 Cambridge, 02139, MA, USA.

14 ³Department of Physics and Technology, University of Bergen,
 15 Bergen, 5020, Norway.

16 ⁴Norwegian Research Center, Postboks 22 Nygårdstangen
 17 Bergen, 5020, Norway.

18 ⁵Center for Modeling of Coupled Subsurface Dynamics,
 19 Department of Mathematics, University of Bergen, Bergen, 5020,
 20 Norway.

21 *Corresponding author(s). E-mail(s): Martin.Ferno@uib.no;
 22 Jan.Nordbotten@uib.no; juanes@mit.edu;

23 Contributing authors: lsalo@mit.edu; Malin.Haugen@uib.no;
 24 Kristoffer.Eikehaug@uib.no;

25 **Abstract**

26 **Purpose:** The accuracy and robustness of numerical models of geo-
 27 logic CO₂ sequestration are almost never quantified with respect
 28 to direct observations that provide a ground truth. This study
 29 presents CO₂ injection experiments in meter-scale, quasi-2D tanks

2 *Simulation of geologic CO₂ storage: Value of Local Data and Forecasting*

30 with porous media representing stratigraphic sections of the sub-
 31 surface, compared to numerical simulations of those experiments.

32 **Goals:** Evaluate (1) the value of prior knowledge of the sys-
 33 tem, expressed in terms of ex-situ measurements of the tank
 34 sands' multiphase flow properties (local data), with respect to
 35 simulation accuracy; and (2) the forecasting capability of the
 36 matched numerical models, when applied to different settings.

37 **Methods:** Match three versions of a numerical simulation model—each
 38 with access to an increasing level of local data—to a CO₂ injec-
 39 tion experiment in Tank 1 ($89.7 \times 47 \times 1.05$ cm). Matching is based
 40 on a quantitative comparison of CO₂ migration at different times
 41 from timelapse image analysis. Next, use the matched models to
 42 make a forecast of a different injection scenario in Tank 1, and,
 43 finally, a different injection scenario in Tank 2 ($2.86 \times 1.3 \times 0.019$
 44 m), which represents an altogether different stratigraphic section.

45 **Results and conclusion:** The simulation model can qualitatively
 46 match the observed free-phase and dissolved CO₂ plume migration
 47 and convective mixing. Quantitatively, simulations are accurate dur-
 48 ing the injection phase but their concordance decreases with time.
 49 Using local data reduces the time required to history match, although
 50 the forecasting capability of matched models is similar. The sand-
 51 water-CO_{2(g)} system is very sensitive to effective permeability and
 52 capillary pressure changes; where heterogeneous structures are present,
 53 accurate deterministic estimates of CO₂ migration are difficult to obtain.

54 **Keywords:** CO₂ storage, geologic carbon sequestration, two-phase flow,
 55 numerical simulations, history matching, FluidFlower

56 1 Introduction

57 CO₂ capture and subsequent geologic carbon sequestration (GCS) is a
 58 climate-change mitigation technology that can be deployed at scale to offset
 59 anthropogenic CO₂ emissions during the energy transition (Marcucci et al.,
 60 2017; European Academies Science Advisory Council (EASAC), 2018; Celia,
 61 2021; Intergovernmental Panel on Climate Change (IPCC), 2022). In GCS,
 62 reservoir simulation, including coupled flow and geomechanics, is the primary
 63 tool used to assess and manage geologic hazards such as fault leakage (e.g.,
 64 Caine et al., 1996; Ingram and Urai, 1999; Nordbotten and Celia, 2012; Zoback
 65 and Gorelick, 2012; Juanes et al., 2012; Jung et al., 2014; Vilarrasa and Car-
 66 rera, 2015; Saló-Salgado et al., 2023) and induced seismicity (e.g., Cappa and
 67 Rutqvist, 2011; Zoback and Gorelick, 2012; Juanes et al., 2012; Ellsworth,
 68 2013; Verdon et al., 2013; Alghannam and Juanes, 2020; Hager et al., 2021). In
 69 response to the inherent uncertainties associated with modeling and simulation
 70 of CO₂ storage (Nordbotten et al., 2012), building confidence in the forecasting
 71 capabilities of simulation models requires calibration (or, synonymously, his-
 72 tory matching), a process that involves updating the reservoir model to match

73 field observations as they become available (Oliver and Chen, 2011; Doughty
74 and Oldenburg, 2020).

75 History matching is an ill-posed inverse problem (Oliver and Chen, 2011).
76 This means that multiple solutions (i.e., parameter combinations) exist that
77 approximate the data equally well. Automated techniques such as Markov
78 chain Monte Carlo, randomized maximum likelihood or ensemble-based meth-
79 ods can be used to quantify uncertainty in history-matched models, especially
80 in combination with surrogate models to reduce forward model computational
81 time (see Aanonsen et al., 2009; Oliver and Chen, 2011; Jagalur-Mohan et al.,
82 2018; Jin et al., 2019; Liu and Durlofsky, 2020; Santoso et al., 2021; Landau-
83 Marbán et al., 2023, forthcoming, and references therein). In practice, however,
84 it may be difficult to ensure that the chosen simulation model provides the best
85 possible forecast. This is due to different subsurface conditions, the inability
86 to include all sources of uncertainty in the models, incomplete field data and
87 limited time for history matching.

88 In the laboratory, intermediate-scale (~meter) experiments have been used
89 to study the physics of petroleum displacement (e.g., Gaucher and Lindley,
90 1960; Brock and Orr, 1991; Cinar et al., 2006) and contaminant trans-
91 port (e.g., Silliman and Simpson, 1987; Wood et al., 1994; Lenhard et al., 1995;
92 Fernández-García et al., 2004). Similar 2D and 3D flow rigs have recently been
93 applied to CO₂ storage, providing a link between core-scale measurements and
94 field observations:

95 Kneafsey and Pruess (2010) found the impact of convective dissolution
96 to be significant, using a page-size Hele-Shaw cell and numerical simula-
97 tions. Neufeld et al. (2010) studied the scaling of convective dissolution and
98 found it to be an important mechanism in the long-term trapping of injected
99 CO₂ in an idealized site. Wang et al. (2010) used a 3D setup to investigate
100 the ability of electrical resistivity tomography to identify localized leaks. Tre-
101 visan et al. (2014, 2017) focused on the impact of structural and residual
102 trapping. In homogeneous sands, they found that previous trapping models,
103 such as the Land (1968) model, can approximate the residually trapped gas
104 saturation ($R^2 > 0.6$). Studying an heterogeneous aquifer characterized by a
105 log-normal distribution of six different sand facies, they report that trapping
106 efficiency increased significantly due to structural trapping. A strong control
107 of sand heterogeneity on upward migration of CO₂ was also found by Lassen
108 et al. (2015). Krishnamurthy et al. (2019, 2022) devised a novel technique to
109 automate the process of beadpack/sandpack deposition and generate realis-
110 tic depositional fabrics; they concluded that grain-size contrast and bedform
111 architecture significantly impact CO₂ trapping. Subsequently, Ni et al. (2023)
112 presented modified invasion-percolation simulations and reported that bed-
113 form architecture can impact CO₂ saturation if enough grain-size contrast is
114 present. Askar et al. (2021) used a ~8 m-long tank to test a framework for
115 GCS monitoring of CO₂ leakage. These studies employed homogeneous glass
116 beads or sands, or focused on heterogeneities and bedform architectures in the
117 aquifer layer; structural complexity was minimal.

4 *Simulation of geologic CO₂ storage: Value of Local Data and Forecasting*

In this paper, we use quasi-2D, intermediate-scale experiments of CO₂ storage to evaluate, quantitatively, the forecasting capability of history-matched simulation models against well-defined spatial data. An attempt was made to recreate realistic basin geometries, including stacking of storage reservoirs, faults, caprock and overburden. We simulate each of the three presented experiments with three versions of a numerical model, each with increasing access to local petrophysical measurements. These different versions are denoted model 1 (M_1), model 2 (M_2) and model 3 (M_3). This allows us to assess (1) the value of local information of the system, expressed in terms of sand petrophysical measurements, during history matching, and (2) transferability or forecasting capability of our matched simulation models, when tested against a different experiment. The term *concordance* is used to evaluate agreement between experiments and observations (Oldenburg, 2018).

131 **2 Physical Experiments**

The physical experiments of CO₂ injection are conducted using the *FluidFlower* rigs. These rigs are meter-scale, quasi-2D tanks with transparent Plexiglass panels designed and built in-house at the University of Bergen (Fig. 1). Here, we used two tanks, with dimensions 89.9 × 47 × 1.05 cm and 2.86 × 1.3 × 0.019 m (referred herein to as Tank 1 and Tank 2, respectively). Different geologic settings are constructed by pouring unconsolidated sands with desired grain sizes into the water-saturated rigs. The rigs have multiple ports which allow flushing out fluids after a given CO₂ injection, such that multiple injections can be conducted in the same setting. The location of the ports can be adjusted to accommodate different injection scenarios. A variety of techniques have been developed by UiB engineers in order to build complex structures such as folds and faults.

Below, we summarize the petrophysical measurements, experimental setup, geologic model/porous media construction and experimental schedule. Details on the conceptualization of the FluidFlower rigs and technical information are given in Fernø et al. (2023, this issue) and Eikehaug et al. (2023, this issue), while the full description of the physical experiment in Tank 1 and ex-situ measurements are provided by Nordbotten et al. (2022); Haugen et al. (2023, this issue). Further details on the experiment in Tank 2, as well as results of the international benchmark study (IBS), are provided by Flemisch et al. (2023, this issue).

153 **2.1 Sand petrophysical properties**

Measurements on the employed Danish quartz sands were conducted using specialized equipment to determine average grain size (d), porosity (ϕ), permeability (k), capillary entry pressure (p_e) and drainage and imbibition saturation endpoints (denoted as connate water saturation, S_{wc} , and trapped gas saturation, S_{gt}). The methodology is described by Haugen et al. (2023, this issue) and obtained values are provided in Tab. 1. Sands C, D, E and F are very

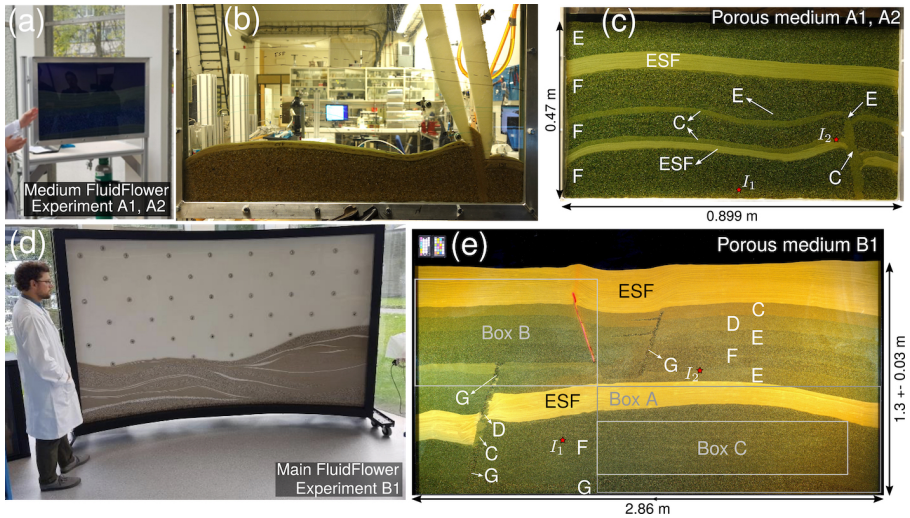


Fig. 1 Overview of the FluidFlower rigs and porous media used in the physical experiments. **a** Medium FluidFlower rig (Tank 1). **b** Snapshot during sand pouring to build the porous medium used in Experiments A1 and A2 in Tank 1 (Haugen et al., 2023, this issue). **c** Front view of porous medium in Tank 1, with lithologies in white and injector location shown with a red star. The length and height correspond to the porous medium. Note the fixed water table at the top. **d** Overview of the main FluidFlower rig (Tank 2), showing the back panel with sensor network. **e** Porous medium in Tank 2, used for Experiment B1, with lithologies in white. Location of injectors and Boxes A, B and C for analysis are shown with a red star and gray boxes, respectively. Length and variable height correspond to the porous medium.

well sorted, sand G is well sorted, and sand ESF is moderately sorted (Haugen et al., 2023, this issue). We verified that Darcy's law is applicable in our system using the Reynolds number (R_e):

$$R_e = \frac{ud}{\nu} \quad (1)$$

where u is the fluid discharge per unit area, d the mean grain diameter, and ν the kinematic viscosity of the fluid. From our simulation results, matched to experimental observations, $\max(R_e) \leq 1$, which ensures the applicability of Darcy's law (e.g., Bear, 1972).

2.2 Experimental setup

The front and back panels of the FluidFlower are mounted on a portable aluminum frame, such that boundaries are closed on the sides and bottom (no flow). The top surface is open and in contact with fluctuating atmospheric pressure (Fig. 1). A fixed water table above the top of the porous medium was kept throughout the experiments conducted here. The experimental setup incorporates mass flow controllers to inject gaseous CO₂ at the desired rate, and a high-resolution digital camera with time-lapse function (Haugen et al., 2023, this issue).

6 *Simulation of geologic CO₂ storage: Value of Local Data and Forecasting*

Table 1 Petrophysical properties for used quartz sands, as obtained from local, ex-situ measurements. Porosity and permeability are the average from two measurements for each sand, with a maximum difference between measurements of 0.02 (ϕ) and estimated 20% uncertainty (k). Measured gas column heights for sands E-G were 0, so p_e could not be directly measured. Experimental error in p_e , S_{wc} and S_{gt} was not quantified. A detailed description of the methodology and petrophysical values is provided by Nordbotten et al. (2022); Haugen et al. (2023, this issue).

Sand type	d (std) [mm]	ϕ [-]	k [D]	p_e [mbar]	S_{wc}	S_{gt}
ESF	0.2 (0.11)	0.435	44	15	0.32	0.14
C	0.66 (0.09)	0.435	473	3	0.14	0.1
D	1.05 (0.14)	0.44	1110	1	0.12	0.08
E	1.45 (0.19)	0.45	2005	-	0.12	0.06
F	1.77 (0.31)	0.44	4259	-	0.12	0.13
G	2.51 (0.63)	0.45	9580	-	0.1	0.06

Experiments were conducted in 2021 and 2022 in Bergen (Norway) at room temperature (≈ 23 °C) and ambient atmospheric pressure. Temperature changes were minimized as much as possible, but maintaining a constant temperature was not possible in the available laboratory space. The fluids and sands were set in the FluidFlowers using the following procedure:

1. The silica sands are cleaned using an acid solution of water and HCl to remove carbonate impurities.
2. The FluidFlower rig is filled with deionized water.
3. Sands are manually poured into the rig using the open top boundary, in order to construct the desired porous medium.
4. A pH-sensitive, deionized-water solution containing bromothymol blue, methyl red, hydroxide and sodium ions is injected through multiple ports until the rig is fully saturated. This enables direct visualization of CO₂ gas (white), dissolved CO₂ (yellowish orange to red), and pure water (dark teal).
5. 5.0 purity (99.999%) CO₂ is injected as gaseous phase at the desired rate. CO₂ is injected through dedicated ports directly into the rig (Fig. 1).
6. After the injection phase, injection ports are closed and CO₂ migration continues.
7. Once the experiment is finished, the rig can be flushed with deionized water and the process can start again from step 4.

Full details on the fluids are given in Fernø et al. (2023, this issue) and Eikehaug et al. (2023, this issue). Below, we refer to the pH-sensitive solution in the rigs as “dyed water”.

2.3 Porous media geometries

The geometries of the porous media used in this paper aim to recreate the trap systems observed in faulted, siliciclastic, petroleum-bearing basins around the world, given the geometrical constraints of the FluidFlowers and manual sand pouring (Fernø et al., 2023; Eikehaug et al., 2023, this issue). Features

such as folds, faults and unconformities were built in both Tanks 1 and 2. The construction of faults, shown in Fig. 1b and detailed in Haugen et al. (2023, this issue), requires a minimum effective “fault-plane” thickness; hence, our fault structures are thicker than natural faults with the same displacement (Childs et al., 2009). Fine sands ($d \approx 0.2$ mm) are used to represent sealing or caprock formations.

The geometry in Tank 1 (Fig. 1c) contains three main high-permeability reservoirs (F sand). The bottom and middle F sand are separated by a seal (ESF sand), while the middle and top are separated by the C sand and connected through a higher permeability fault (refer to sect. 2.1 for petrophysical properties). The fault separates the bottom section into two compartments. The bottom and top F sand provide anticlinal traps for the CO₂ to accumulate in.

The geometry in Tank 2 (Fig. 1e) was specifically motivated by the structure of North Sea reservoirs and petroleum basins. From bottom to top, it contains two sections of decreasing-permeability reservoirs capped by two main sealing layers. A fault separates the bottom section into two compartments, while two faults separate the top section into three compartments. Each fault has different petrophysical properties: The bottom fault is a heterogeneous structure containing ESF, C, D, F and G sands, the top-left fault is an impermeable structure made of silicone and the top-right fault is a conduit structure containing G sand.

2.4 Experimental injection schedule

The injection schedules for experiments in Tanks 1 and 2 are provided in Tab. 2. Injection ports have an inner diameter of 1.8 mm.

Table 2 Schedules for the three CO₂ injection experiments simulated in this work. I_R is injection rate, while I_i denotes injector (port) number. A five-minute ramp-up and ramp-down was applied in Experiments A1 and A2 in Tank 1. Total duration of conducted experiments and simulations is 48h (A1), 5h (A2) and 120h (B1). Location of injection wells is provided in Fig. 1.

Experiment A1		A2		B1	
I_R [ml/min]	t [hh:mm:ss]	I_R	t	I_R	t
0.1 (I_1)	00:00:00	0.1 (I_1)	00:00:00	10.0 (I_1)	00:00:00
2.0	00:05:00	2.0	00:05:00	10.0	05:00:00
2.0	00:50:00	2.0	04:43:44	0.0	05:00:01
0.0	00:55:00	0.0	04:48:33	10.0 (I_2)	02:15:00
0.1 (I_2)	01:09:11	0.0	05:00:00	10.0	05:00:00
2.0	01:14:11			0.0	05:00:01
2.0	02:29:11			0.0	120:00:00
0.0	02:34:00				
0.0	48:00:00				

230 3 Numerical simulations

231 3.1 Model setup

232 The isothermal simulations presented in this work were performed with the
 233 MATLAB Reservoir Simulation Toolbox, MRST (Krogstad et al., 2015; Lie,
 234 2019; Lie and Møyner, 2021). Specifically, we used the black-oil module, which
 235 is based on fully implicit solvers with automatic differentiation, and assigned
 236 properties of water to the oleic phase, such that the gaseous phase (CO₂
 237 only) can dissolve in it. Vaporization of water into the gas phase and chemical
 238 reactions are not considered, because they are not primary controls on fluid
 239 migration for our operational setup and analysis time.

240 In addition to structural and dissolution trapping, we also considered residual
 241 trapping (Juanes et al., 2006) to be consistent with local measurements
 242 showing nonzero trapped gas saturation (sect. 2.1). This is achieved through
 243 hysteretic relative permeability curves for the nonwetting (gas) phase (see
 244 sect. 3.2). Our implementation in MRST follows ECLIPSE's technical descrip-
 245 tion (Schlumberger, 2014), and Killough's (1976) model is used to compute
 246 the scanning curves (Saló-Salgado et al., 2023, forthcoming). Physical diffusion
 247 was also included through the addition of a diffusive flux term with a scalar,
 248 constant coefficient in the computation of the total CO₂ flux (Bear, 1972).

249 The simulator requires very small time-steps (seconds to minutes) due to
 250 the buoyancy of CO₂ at atmospheric conditions and high sand permeabilities
 251 (Tab. 1). Linear solver time was reduced by means of AMGCL (Demidov and
 252 Rossi, 2018; Lie, 2019), an external, pre-compiled linear solver. The greatest
 253 challenge was the convergence of the nonlinear solver, which required many
 254 iterations and time-step cuts. This is consistent with the groups working in the
 255 FluidFlower international benchmark study (Flemisch et al., 2023, this issue).

256 Next, we describe the computational grids for experiments in Tanks 1 and 2,
 257 PVT properties and boundary conditions. Petrophysical properties are specific
 258 of each model version and are detailed in sect. 3.2.

259 3.1.1 Computational grids

260 A front panel image of the porous medium was used to obtain layer contact
 261 coordinates through a vector graphics software (Fig. 2a). These contacts were
 262 then imported into MATLAB to generate the computational grids using the
 263 UPR module (Berge et al., 2019, 2021)(Fig. 2b,d). The grids were generated in
 264 2D and then extruded to 3D (using a single cell layer) to account for thickness
 265 and volume. Note that, in Tank 1, where the porous medium has dimensions
 266 of 89.7 × 47 × 1.05 cm, the thickness (space between the front and back panels)
 267 is constant (10.5 mm). Tank 2, which is significantly larger (porous medium
 268 dimensions 2.86 × 1.3 × 0.019 m), has a thickness of 19 mm at the sides; however,
 269 it varies towards the middle due to forces exerted by the sand and water, to
 270 a maximum of 28 mm. A thickness map obtained after initial sand filling was
 271 used to generate our variable-thickness mesh via 2D interpolation (Fig. 2c).
 272 Also, the top surface of the porous medium is not flat (height = 130 ± 3 cm).

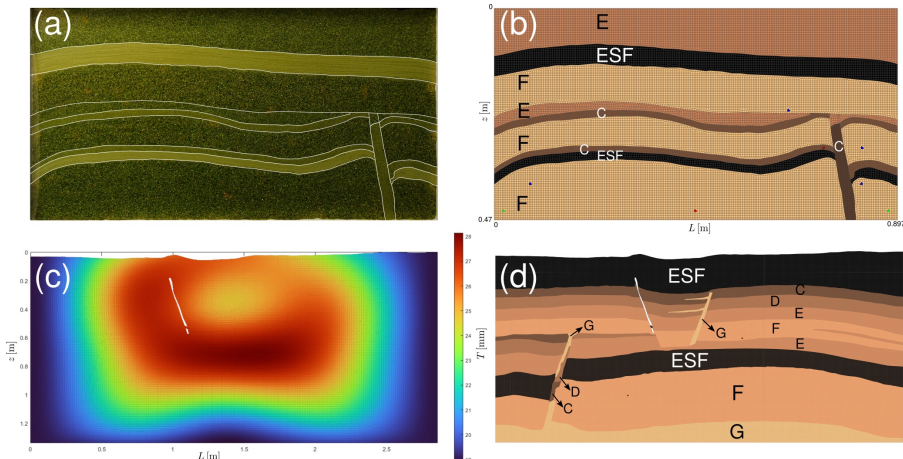


Fig. 2 Simulation grids overview. **a** front panel view of Tank 1, where the layer contacts have been highlighted in white. **b** front view of simulation grid for experiments in Tank 1, with lithologies indicated and colored based on petrophysical properties (see sect. 3.2). Location of injection wells is shown in red. **c** thickness map of simulation grid for experiments in Tank 2. **d** front view of simulation grid for experiments in Tank 2, with lithologies indicated and colored based on petrophysical properties. Location of injection wells is shown in red.

Our composite Pebe grids (Heinemann et al., 1991) have a Cartesian background and are refined around face constraints (contacts and faults) as well as cell constraints (injection wells) (Berge et al., 2019, 2021). We generated multiple grids to test the finest grid we could afford to simulate Experiment B1 in Tank 2 with. Our grid has a cell size $h \approx 5$ mm and 151,402 cells (Fig. 2d). The grid used for Tank 1 has a similar cell size ($h \approx 4$ mm and 27,200 cells), which was chosen to reduce grid-size dependencies when applying our matched models to Experiment B1.

3.1.2 PVT properties

Consistent with experimental conditions, our simulations are conducted at atmospheric conditions ($T = 25$ °C), where the CO₂ is in gaseous state. We employed a thermodynamic model based on the formulations by Duan and Sun (2003) and Spycher et al. (2003); Spycher and Pruess (2005) to calculate the composition of each phase as a function of p , T . The implementation for a black-oil setup is described in Hassanzadeh et al. (2008) and references therein. Given the boundary conditions (sect. 3.1.3) and dimensions of our experimental porous media, pore pressure changes (Δp) are very small in our simulations ($\max \Delta p \ll 1$ bar). Hence, the fluid properties remain similar to surface conditions, where the water and CO₂ have, respectively, a density of 997 and 1.78 kg/m³, and a viscosity of 0.9 and 0.015 cP. The maximum concentration of CO₂ in water is ≈ 1.5 kg/m³.

294 **3.1.3 Initial, boundary and operational conditions**

295 Our porous media are fully saturated in water at the beginning of CO₂ injection.
 296 No-flow boundary conditions were applied everywhere except at the top
 297 boundary, which is at constant pressure and includes a fixed water table a
 298 few cm above the top of the porous medium. Injection is carried out via wells
 299 completed in a single cell at the corresponding coordinates. The diameter of
 300 injection wells is 1.8 mm in both Tank 1 and Tank 2, which operate at a
 301 constant flow rate (see sect. 2). The simulation injection schedule follows the
 302 experimental protocol, provided in Tab. 2. Note that injection rates in our sim-
 303 ulations of Experiment A1 and A2 were slightly adjusted during the calibration
 304 procedure, as explained in sect. 3.3 and 4.

305 **3.2 Simulation model**

306 Three different model versions, denoted model 1 (M_1), model 2 (M_2) and model
 307 3 (M_3), are used throughout this study to evaluate the value of local data in
 308 forecasting subsurface CO₂ migration. Each successive model was constructed
 309 based on access to an increasing level of local data, with M_1 having access
 310 to the least data and M_3 having access to the most data. The model-specific
 311 parameters are limited to the following:

- 312 • Petrophysical properties (porosity, permeability, capillary pressure and rel-
 313 ative permeability), which depend on available local data and are described
 314 in this section.
- 315 • The molecular diffusion coefficient (D). Models 1-3 were calibrated using
 316 the same value, $D = 10^{-9}$ m²/s. Additionally, model 3 was also calibrated
 317 with $D = 3 \times 10^{-9}$ m²/s. Accordingly, where required we denote model 3 as
 318 $M_{3,1}$ and $M_{3,3}$.
- 319 • Injection rate. Experiments in Tank 1 were conducted at a very low injection
 320 rate ($I_R = 2$ ml/min, see Tab. 2). Given that the mass flow controllers
 321 used in Tank 1 may be inaccurate for this rate, the injection rate was also
 322 modeled as an uncertain parameter. Model calibration was achieved with
 323 $I_R \in [1.6, 1.8]$ ml/min for all three models.

324 All other model characteristics, including the grid and numerical discretiza-
 325 tion, remain unchanged. Below, we describe the starting petrophysical values
 326 for each of our three simulation models. Note that the experimental geom-
 327 etry in Tank 1, used for matching, only contained sands ESF, C, E and F.
 328 Properties for sands D and G are also provided because they were required to
 329 simulate the experiment in Tank 2 (Fig. 1).

330 **3.2.1 Model 1 (M_1)**

331 For this model, local petrophysical data were limited to a measure of the aver-
 332 age grain size (d ; see sect. 2.1 and Tab. 1). Hence, petrophysical properties were
 333 estimated from published data in similar silica sands. Porosity was selected
 334 from data in Beard and Weyl (1973) and Smits et al. (2010) for moderately to

335 well-sorted sands. Permeability was obtained from fitting a Kozeny-Carman
 336 model to data in Beard and Weyl (1973) and Trevisan et al. (2014). The result-
 337 ing equation has the form $k = \beta d^2 \phi^3$, where β equals 12,250 in our fit with d
 338 in mm and k in D. Obtained porosity and permeability values are provided in
 339 Table 3.

Table 3 Initial porosity and permeability for model 1. See main text for estimation details.

Sand type	d [mm]	ϕ [-]	k [D]
ESF	0.2	0.37	25
C	0.66	0.38	290
D	1.05	0.40	930
E	1.45	0.39	1530
F	1.77	0.39	2280
G	2.51	0.42	5720

340 Capillary pressure curves were computed as described below:

- 341 1. Capillary pressure measurements in a similar system were obtained from
 342 the literature. In this case, Plug and Bruining (2007) measured capillary
 343 pressure curves on the unconsolidated quartz sand-CO₂-distilled water sys-
 344 tem at atmospheric conditions. We used their measurements on sand packs
 345 with an average particle size between 0.36 and 0.41 mm, which are closest
 346 to the C sand in our experiments (Fig. 3a).
- 347 2. A Brooks and Corey (1964) model of the form $p_c = p_e(S_w^*)^{-\frac{1}{\lambda}}$ was fitted to
 348 these data, where p_e is the nonwetting phase entry pressure at $S_w = 1$, $\lambda =$
 349 2.6 and $S_w^* = \frac{S_w - S_{wc}}{1 - S_{wc}}$ is the normalized water saturation with irreducible
 350 or connate water saturation S_{wc} . This fit led to our reference curve, p_{cr}
 351 (Fig. 3a).
- 352 3. The capillary pressure depends on the pore structure of each material, such
 353 that sands with different grain sizes require different p_c curves. The capillary
 354 pressure variation can be modeled by means of the dimensionless J -function
 355 proposed by Leverett (Leverett, 1941; Saadatpoor et al., 2010): $J(S_w) =$
 356 $\frac{p_c}{\sigma \cos \theta} \sqrt{\frac{k}{\phi}}$, where σ is the surface tension and θ the contact angle. Assuming
 357 the same wettability and surface tension for different sand regions, and
 358 the same shape of the p_c curve, the capillary pressure for any given sand
 359 (p_{cs}) can be obtained from the reference curve as $p_{cs}(S_w) = p_{cr}(S_w) \sqrt{\frac{k_r \phi_s}{k_s \phi_r}}$
 360 (Fig. 3b).

361 Drainage relative permeabilities were obtained from CO₂-water measure-
 362 ments by DiCarlo et al. (2000), who used water-wet sandpacks with 0.25 mm
 363 grain size. Specifically, we used the data reported in their Fig. 4 and 5, and
 364 fitted Corey-type functions (Corey, 1954; Brooks and Corey, 1964) of the form
 365 $k_{rw} = (S_w^*)^a$ and $k_{rg} = c(1 - S_w^*)^b$ (Fig. 3c). The fitted exponents a and b
 366 are 4.2 and 1.4, respectively, while c is 0.97. We assumed that the difference
 367 in relative permeability of different sands is the result of different irreducible

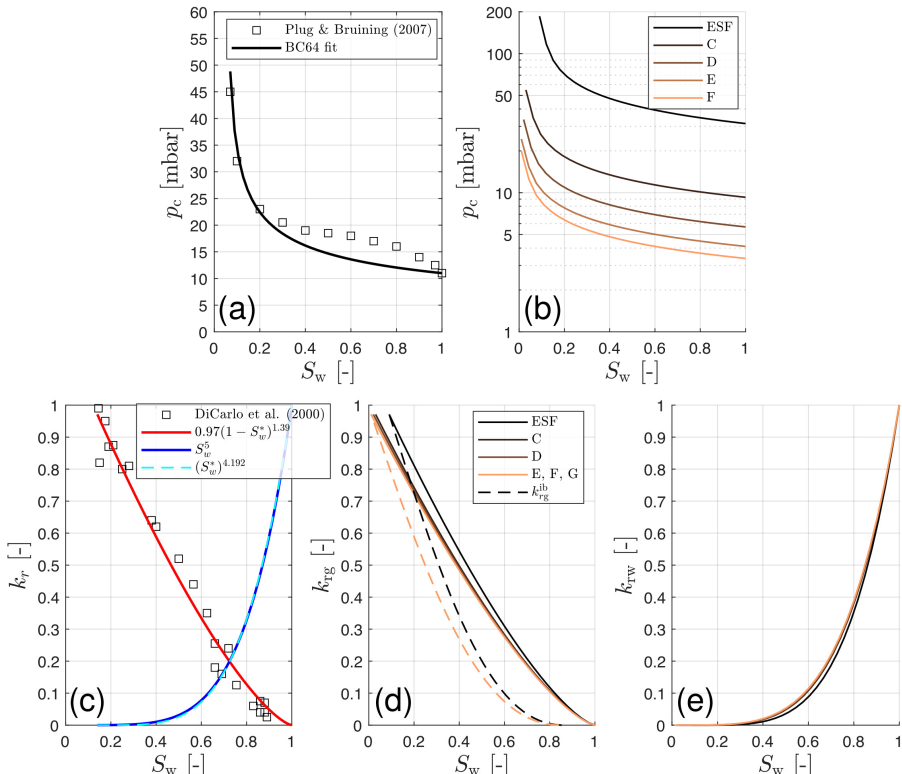


Fig. 3 Multiphase flow properties for model 1. **a** Capillary pressure measurements and reference curve using a Brooks and Corey (1964) function. **b** Initial capillary pressure curves, computed from the reference curve using Leverett scaling (see main text). **c** Relative permeability data (squares and S_w^5 model) and our fitted Corey model. **d,e** Relative permeability of gas and water, respectively. The drainage curve is shown as a solid line, while the bounding imbibition curve is shown for sands ESF and G as a discontinuous line. No relative permeability hysteresis was considered for the water phase.

water saturation only (see Fig. 3d,e). For each of our sands, S_{wc} was obtained from Timur (1968) as $S_{\text{wc}} = 0.01 \times 3.5 \frac{\phi^{1.26}}{k^{0.35}} - 1$, where ϕ is in percent and k in mD. This model was used to compute S_{wc} for both the p_c and k_r curves.

In CO₂ storage, secondary imbibition occurs where the water displaces buoyant gas at the trailing edge of the CO₂ plume, disconnecting part of the CO₂ body into blobs and ganglia and rendering them immobile (Juanes et al., 2006, and references therein). This means that the maximum water saturation that can be achieved during imbibition equals $1 - S_{\text{gt}}$ (the trapped gas saturation). Here, we used measurements in sandpacks from Pentland et al. (2010) to determine S_{gt} . In particular, we fitted Land (1968)'s model with the form $S_{\text{gt}}^* = \frac{S_{\text{gi}}^*}{1 + CS_{\text{gi}}^*}$, where $S_{\text{g}}^* = \frac{S_{\text{g}}}{1 - S_{\text{wc}}} = 1 - S_{\text{w}}^*$, S_{gi} is the gas saturation at flow reversal, and C is Land's trapping coefficient with a value of 5.2 in our fit. Although Pentland et al. (2010) report that the best fit is achieved with

the Aissaoui (1983) and Spiteri et al. (2008) models (cf. their Fig. 5), Land's model was chosen here given that most relative permeability hysteresis models build on this one (see next paragraph).

Nonwetting phase trapping contributes to irreversibility of the relative permeability and capillary pressure curves (hysteresis). Here, we accounted for this mechanism in the gas relative permeability due to its importance in subsurface CO₂ migration (Juanes et al., 2006, and references therein). In particular, we used Land's (1968) model to compute the bounding imbibition curve (see Fig. 3d), where S_{gt} is obtained as described above, and Killough's (1976) model to characterize the scanning curves. In Killough's model, the scanning curves are reversible, such that the relative permeability at $S_g < S_{gi}$ no longer depends on the displacement type.

3.2.2 Model 2 (M_2)

This model had access to local, ex-situ measurements of single-phase petrophysical properties, i.e., porosity and intrinsic permeability (see sect. 2.1 and Tab. 1). Comparing with Tab. 3, it can be seen that our estimation for model 1 above was correct to the order of magnitude, but resulted in smaller values: porosity $\in [85, 93]\%$ and permeability $\in [53, 84]\%$ of the local measurements.

Capillary pressures and relative permeabilities were obtained using the same procedure described above for model 1. The slight differences with respect to the curves shown in Fig. 3b,d,e come from the porosity and permeability values used in the Leverett scaling and to determine S_{wc} , which were taken from Tab. 1 instead. The obtained curves for model 2 are provided in Fig 4.

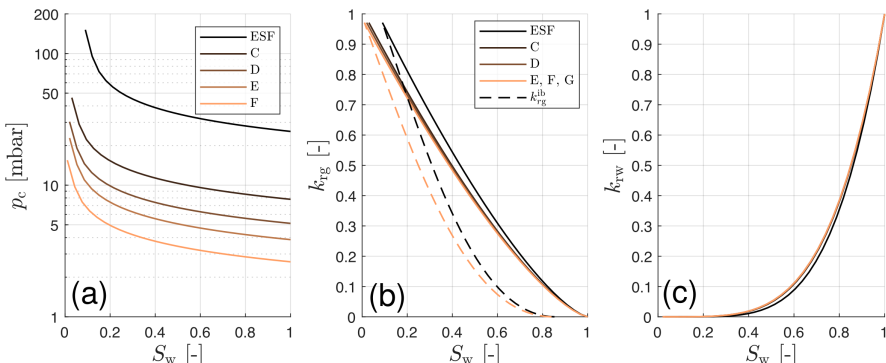


Fig. 4 Multiphase flow properties for model 2. **b** Initial capillary pressure curves, computed from the reference curve using Leverett scaling (see main text). **b,c** Relative permeability of gas and water, respectively. The drainage curve is solid, while the bounding imbibition curve is shown for sands ESF and G as a discontinuous line. No relative permeability hysteresis was considered for the water phase.

404 3.2.3 Model 3 (M_3)

405 This model was allowed access to all local, ex-situ measurements (see Tab. 1).
 406 Initial porosity and permeability remain unchanged with respect to model
 407 2. Capillary pressure curves were obtained by scaling the reference curve
 408 described in sect. 3.2.1 and shown in Fig. 3a using the measured entry pres-
 409 sure (sect. 2.1). The scaling followed the model $p_{cs}(S_w) = p_{cr}(S_w) \frac{p_e}{p_{per}}$, where
 410 p_e is the measured entry pressure for each sand, and p_{er} is the reference curve
 411 entry pressure. The obtained curves are shown in Fig. 5a.

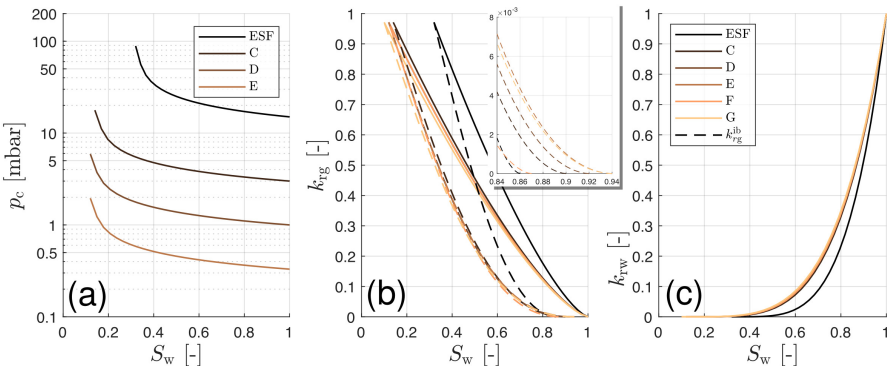


Fig. 5 Multiphase flow properties for model 3. **b** Initial capillary pressure curves, computed according to the entry pressure determined experimentally (see sect. 2.1). **b,c** Relative permeability of gas and water, respectively, according to the endpoints determined experimentally (sect. 2.1). The drainage curves are solid, while the bounding imbibition curves are shown as a discontinuous line. The inset in **b** is a zoom view around the trapped gas saturation. No relative permeability hysteresis was considered for the water phase.

412 Relative permeabilities were computed following the same procedure
 413 described for model 1 above. In this case, however, each sand type was assigned
 414 the measured S_{wc} and S_{gt} values (see Tab. 1). This led to differences in both
 415 the drainage and imbibition curves, as shown in Fig. 5.

416 3.3 Model calibration

417 Concordance between results obtained with each simulation model (1 to 3)
 418 and the validation experiment in Tank 1 (A1, see sect. 2.4) is quantitatively
 419 assessed by comparing the following quantities (see Fig. 6):

- 420 1. At $t = 55$ min (end of injection in port I_1): Areas occupied by free-phase
 421 CO₂, and dyed water with dissolved CO₂ in the bottom F reservoir.
- 422 2. At $t = 154$ min (end of injection in port I_2): Areas occupied by free-phase
 423 CO₂, and dyed water with dissolved CO₂, in the middle and top F reservoirs.
- 424 3. Time at which the first finger touches the tank bottom.
- 425 4. Time at which the first finger (sinking from the top F reservoir) touches
 426 the middle C sand.

427 Experimental values for points 1-2 were obtained by computing areas from
 428 time-lapse images using a vector-graphics software. Careful visual inspection of
 429 color-enhanced images was used to distinguish between free-phase CO₂ (white)
 430 and dyed water with dissolved CO₂ (yellowish orange to red), and to identify
 431 the times for points 3-4 above. Error in experimental values was estimated
 432 to be $\leq 5\%$, based on repeated measurements (points 1-2), and ~ 5 min,
 433 based on timelapse image comparison (points 3-4). In the simulation models,
 434 the threshold gas saturation and CO₂ concentration in water used to compute
 435 areas were $S_g > 10^{-3}$ and $C_{CO_2} > 15\% (C_{CO_2}^{\max}) \approx 0.2$ [kg/m³], respectively.
 436 The C value was chosen after a shape comparison of the region with dissolved
 437 CO₂. A smaller value of $C_{CO_2} > 0.05$ [kg/m³] was selected to determine finger
 438 times for points 3 and 4 above. Fig. 6 shows an overview of the experimental
 439 values for points 2 and 3, while Fig. 12 in Sect. 4.2 shows the full comparison
 440 with the history-matched/calibrated simulation models.

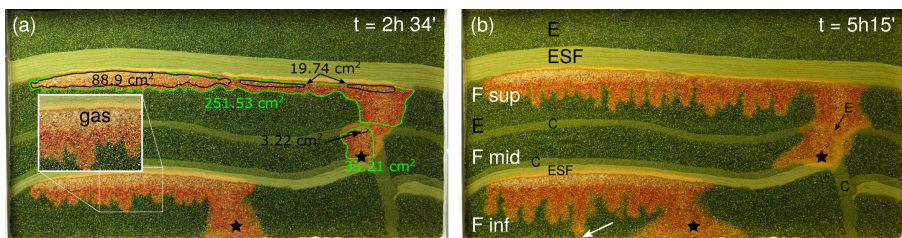


Fig. 6 Front panel view of Tank 1, showing quantities and times for history matching of numerical models to Experiment A1. **a** shows areas with gaseous CO₂ (free-phase, black contours) and dyed water with dissolved CO₂ (green contours) at the end of injection. Location of injection ports is shown with a star. **b** shows the time and location where the first finger touches the bottom of the tank (white arrow), as well as the different lithological units. Note the three F reservoirs labeled ‘inf’, ‘mid’ and ‘sup’, mentioned in the text and other figures.

441 The experiment was conducted first. Afterwards, the process consisted of
 442 running simulation models 1 to 3, in parallel, starting with the petrophysical
 443 properties described in sect. 3.2. Given the number of uncertain variables (four
 444 petrophysical properties for each lithological unit, the diffusion coefficient and
 445 the injection rate) and the time required to complete a single simulation, a
 446 manual history matching method was employed. At the end of each run, quan-
 447 tities 1-4 above were compared and one or more properties were manually
 448 changed based on observed concordance and domain knowledge. During the
 449 first few runs, only quantities 1 and 2 above were compared. After obtaining
 450 a satisfactory areal match, petrophysical properties were further adjusted to
 451 match quantities 3 and 4.

4 Results

452 In sect. 4.1, we present the results of the first simulation of Experiment A1
 453 with each model and property values detailed in sect. 3.2. Then, we detail the

16 *Simulation of geologic CO₂ storage: Value of Local Data and Forecasting*

455 calibration of simulation models using Experiment A1, and assess the value of
 456 local data to history-match CO₂ storage simulation models (sect. 4.2). Finally,
 457 we apply these matched models to Experiment A2, analog for a longer injection
 458 in the same geology (sect. 4.3.1), and to Experiment B1, analog for a larger-
 459 scale injection in a different geologic setting (sect. 4.3.2). We use simulations of
 460 Experiments A2 and B1 to assess the forecasting ability of simulation models
 461 in different conditions.

462 **4.1 Initial model results**

463 Fig. 7 shows the comparison between Experiment A1 and the first run with
 464 each model, at times indicated in sect. 3.3. Numerous differences are evident
 465 between the experiment and models 1 and 2, while model 3 is much closer to
 466 the experiment. In particular, models 1 and 2 overestimate the extent of CO₂-
 467 rich brine and underestimate the amount of gaseous CO₂ in all F reservoirs
 468 (refer to Fig. 6 for location). Model 3 approximates much better the areal
 469 extent of gaseous CO₂ in all regions, as well as the CO₂-rich brine in the middle
 470 and upper F reservoirs. Model 2 provides the closest finger migration times
 471 (points 3 and 4 in sect. 3.3), although this was not evaluated in the first run,
 472 as discussed below.

473 Petrophysical properties for models 1 and 2 were obtained from references
 474 in sect. 3.2, which also used silica sands with similar grain sizes. However,
 475 despite the relatively homogeneous nature of our quartz sands, model 3 is signifi-
 476 cantly more concordant. This result stems from natural sand variability
 477 and highlights the difficulty in establishing general, representative elementary
 478 volume-scale properties for porous media (see, for instance, Hommel et al.,
 479 2018; Schulz et al., 2019, for a discussion on intrinsic permeability). Addi-
 480 tionally, results in Fig. 7 highlight the need for conducting sand/rock-specific
 481 measurements, even in the case of well-sorted, homogeneous sediments.

482 **4.2 Manual history matching and value of local data**

483 Fig. 8 shows convergence of areas occupied by free gas (A_g) and water with
 484 dissolved CO₂ (A_d), according to sect. 3.3. Each iteration corresponds to a
 485 successive model with manually updated parameters, and the different F sand
 486 regions evaluated in each panel (a) to (f) are provided in Fig. 6. With the
 487 exception of A_d in the upper compartment, model 3 is accurate since the
 488 beginning, and all areas were satisfactorily matched after four iterations. Con-
 489 versely, model 1 and 2 were significantly off the experimental reference during
 490 the first few iterations. Model 2, however, was accurate after five iterations,
 491 while model 1 required seven iterations to give satisfactory areal estimates. The
 492 mean absolute error (MAE) over the six areal quantities presented in Fig. 8 is
 493 evaluated in Fig. 9, where it can be seen that, while all models are accurate
 494 towards the end (MAE $\in [5 - 10] \text{ cm}^2$), that required a six-fold improvement
 495 in models 1 and 2, but only two-fold in model 3. As mentioned in sect. 3.3,
 496 $C_{\text{CO}_2} > 15\% (C_{\text{CO}_2}^{\max}) \approx 0.2 \text{ [kg/m}^3]$ was used as threshold to determine areas.

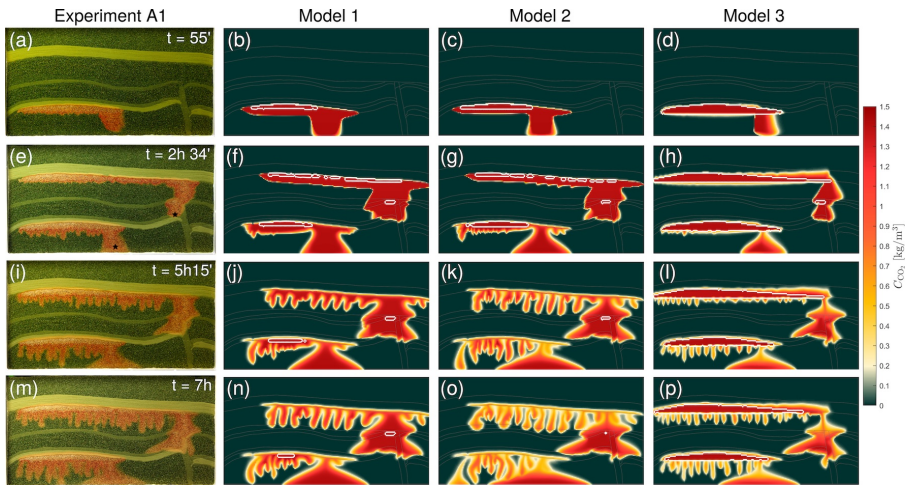


Fig. 7 Comparison between Experiment A1 in Tank 1 (left column) and first run simulation results with models 1–3. Color map in simulation plots refers to CO₂ concentration in water, according to color bar. The white contours in simulation plots indicate $S_g = 10^{-3}$. **a-d:** end of injection in port 1. **e-h:** end of injection in port 2. **i-l:** time at which the first finger touches the tank bottom. **m-p:** time at which the first finger touches the middle C sand.

While the absolute values and error would change with a different C_{CO_2} threshold, we checked that the relative accuracy of our calibrated models does not with both $C_{CO_2} > 0.01$ and 0.1 [kg/m³].

Agreement between simulations and experimental observations is readily seen in Fig. 10, where the 1:1 line indicates perfect concordance. The degree of concordance can be quantified by means of Lin's concordance correlation coefficient (CCC) (Lin, 1989; Oldenburg, 2018), which, for N -valued observation (x) and model (y) vectors (the six areal quantities) is computed as:

$$CCC = \frac{2\sigma_{xy}}{\sigma_x^2 + \sigma_y^2 + (\bar{x} - \bar{y})^2} \quad (2)$$

Where \bar{x} and \bar{y} are the means, σ_x^2 and σ_y^2 the variances, and σ_{xy} the covariance, all calculated using $1/N$ normalization. Results in Fig. 10 show that model calibration results in very good concordance for all models ($CCC \geq 0.99$).

Convergence of quantities 3 and 4 in sect. 3.3, the times at which the first finger touches the rig bottom and the middle C sand, respectively, are provided in Fig. 11. These times were only evaluated after a satisfactory areal match for quantities in Fig. 8 was achieved. Therefore, areas no longer change much in the last few iterations in Fig. 8. In Fig. 11, it can be seen that model 2 and 3, which incorporated local intrinsic permeability measurements, were significantly closer to our experimental reference than model 1. Initially, however, we observed that sinking of gravity fingers in the experiment was faster than our model values by a factor of ≈ 2 . A satisfactory match of all quantities evaluated was achieved after 11, 8, and 7 iterations for models 1–3, respectively.

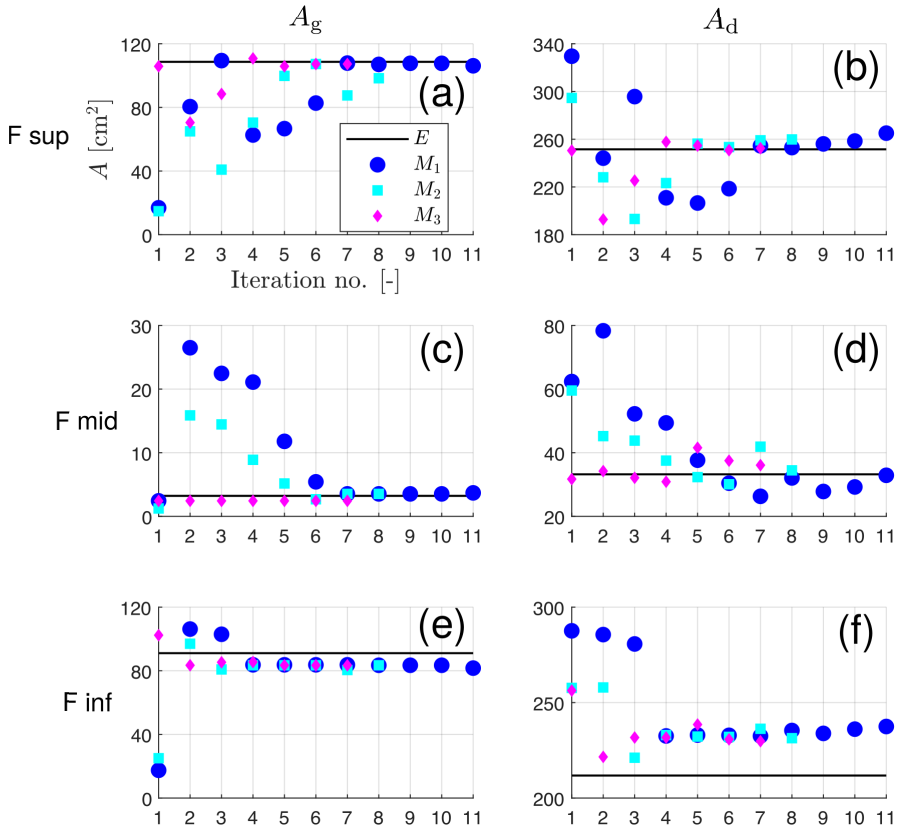


Fig. 8 Convergence of areas occupied by free gas (A_g , left column) and water with dissolved CO₂ (A_d , right column), during the calibration of models 1–3 with Experiment A1. A_d includes area with gaseous CO₂ (see Fig. 6). Each iteration represents a new simulation run, and the experimental reference (E) is shown as a black line. Refer to Fig. 6 for region location, and to sect. 3.3 for calibration procedure. **a,b:** upper F sand. **c,d:** middle F sand. **e,f:** lower F sand.

Overall, we find that model 3, with access to local single-phase and multiphase flow properties, is closer to the experimental reference (i.e., more concordant) from the start. Model 1 started farthest, and required significantly more effort for calibration. After the calibration process, all models achieve very good concordance (CCC ≥ 0.99), based on evaluated quantities (Fig. 10). The calibration shown in Fig. 8, 9, 10, 11 employs $D = 10^{-9}$ m²/s in all model versions (M_1 to M_3). Injection rates (I_R) started at 2.0 ml/min for all three models, and were 1.6 ml/min, 1.8 ml/min and 1.75 ml/min, respectively, at the end of the calibration. I_R is slightly different because the goal was to obtain the best match with each model, considering I_R to be an uncertain variable. In sect. 4.3 below, the same I_R is used to make forecasts with all three models.

Tab. 4 compares the starting and final (matched) key petrophysical variables for each model. The models were successfully calibrated by adjusting

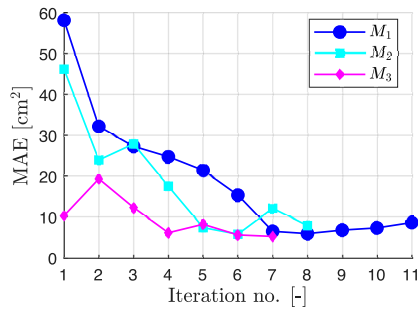


Fig. 9 Convergence of mean absolute error over the six areal quantities measured during the calibration process. The error is computed with respect to experimental values. See Fig. 8 for areas measured, and refer to sect. 3.3 for calibration procedure.

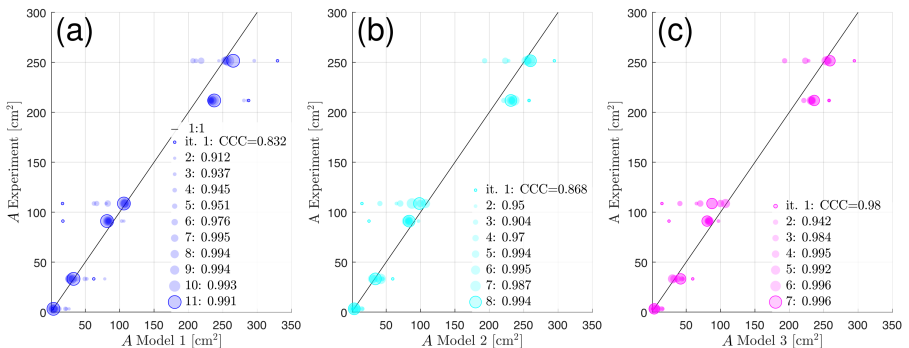


Fig. 10 Concordance between successive model iterations and the experiment, based on six areal measures evaluated during the calibration. Lin's CCC (Lin, 1989) is shown in the key of each subplot, computed according to Eq. 2. **a:** Model 1. **b:** Model 2. **c:** Model 3.

intrinsic permeability and the capillary pressure curves (same shape, but scaled to higher or lower p_e) only. It was found that CO₂ migration was most sensitive to the properties of the F sand, were most of the CO₂ migration occurs, as well as the ESF seal, which structurally traps the CO₂ plume. In our matched models, p_e of ESF is about twice the measured value; this was required because the minimum saturation at which we can define p_e and ensure numerical convergence is $S_g \approx 10^{-4}$. Reality, however, is closer to a jump in p_c from 0 to p_e at an infinitesimally small S_g . Additionally, we found that concordance improved when using different values for the C and F sands in different model regions. In the case of the C sand, the explanation lies in the fault construction process, which may reduce porosity with respect to “natural” sedimentation of stratigraphic layers (Haugen et al., 2023, this issue). The increase in F sand permeability was required to match finger migration times, and is possibly compensating the absence of mechanical dispersion in the simulations. This is

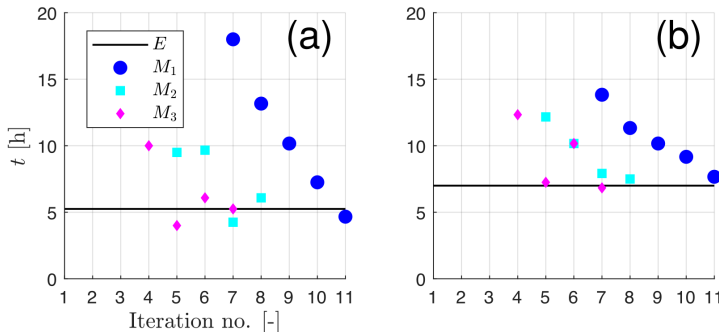


Fig. 11 Convergence of times at which the first finger touches the bottom of the rig (a) and the middle C sand (b), during the calibration of models 1-3 with Experiment A1. Refer to sect. 3.3 for calibration procedure.

discussed in sect. 5. Our calibrated values are within the same order of magnitude of the ex-situ measurements (Tab. 4) and history-matched values for the porous medium in Tank 2 (Landa-Marbán et al., 2023, forthcoming).

Fig. 12 shows gas saturation (S_g) and CO₂ concentration (C_{CO_2}) maps at times at which quantities 1-4 described in sect. 3.3 are evaluated. Snapshots are provided for model 3 only, since all three calibrated models were qualitatively very similar. It can be seen that CO₂ migration is successfully approximated by our numerical model. In detail, however, some differences are apparent: Firstly, sinking of CO₂-rich water from the bottom injector and horizontal migration along the bottom of the rig is faster in the model. This is due to the higher permeability that our numerical model requires in order to match the gravity fingering advance (cf. Tab. 4). Secondly, the experiment shows that denser, CO₂-rich water sinks with a rather compact front and closely spaced, wide fingers. Our model with constant $D = 10^{-9} \text{ m}^2/\text{s}$ approximates all gravity-driven migration of the CO₂-rich water through thinner fingers, with the CO₂-saturated region receding with S_g . To better represent fingering widths, we also matched model 3 with $D = 3 \times 10^{-9} \text{ m}^2/\text{s}$, used in sect. 4.3.2.

4.3 Transferability: model forecasts

A key question after history matching a flow simulation model is whether the physical description has actually been improved, or whether parameters have been modified to match a set of specific observations only. By applying the history-matched models to a different injection protocol (Experiment A2 in Tank 1; refer to Tab. 2), and subsequently to a different geometry (Experiment B1 in Tank 2), this can be assessed to some extent.

4.3.1 Analog for a longer CO₂ injection in the same geologic setting

This case illustrates concordance of our history matched models in a much longer injection in the same geology (Experiment A2). Before simulating this

Table 4 Petrophysical properties for used quartz sands in Experiment A1. Methodology for local measurements is provided by Haugen et al. (2023), while starting property modeling is described in sect. 3.2. For each sand, measured (first row), initial (superscript i) and final (superscript f) values for each of our models is shown. For sand C, the second permeability value refers to the fault, if different from the rest. For sand F, the second permeability value refers to the middle F layer, if different from the rest. For model 3, where property values are different, $M_{3,1}$ refers to the calibration with $D = 10^{-9}$ m²/s and $M_{3,3}$ refers to $D = 3 \times 10^{-9}$ m²/s.

Sand type / model	ϕ [-]	k [D]	p_e [mbar]	S_{wc} [-]	S_{gt} [-]
ESF	0.435	44	15	0.32	0.14
M_1^i	0.37	25	31.4	0.09	0.1468
M_1^f	0.37	6	31.4	0.09	0.1468
M_2^i	0.435	44	25.6	0.09	0.1468
M_2^f	0.435	44	25.6	0.09	0.1468
M_3^i	0.435	44	15	0.32	0.14
M_3^f	0.435	15	30	0.32	0.14
C	0.435	473	3	0.14	0.1
M_1^i	0.38	293	9.3	0.03	0.1565
M_1^f	0.38	293, 27	4.6	0.03	0.1565
M_2^i	0.435	473	7.8	0.03	0.1565
M_2^f	0.435	473, 158	2.6	0.03	0.1565
M_3^i	0.435	473	3	0.14	0.1
M_3^f	0.435	473, 118	4.5	0.14	0.1
E	0.45	2005	-	0.12	0.06
M_1^i	0.39	1528	4.1	0.01	0.16
M_1^f	0.39	1528	0.5	0.01	0.16
M_2^i	0.45	2005	3.86	0.01	0.16
M_2^f	0.45	3008	0.58	0.01	0.16
M_3^i	0.45	2005	0.33	0.12	0.06
$M_{3,1}^f$	0.45	2406	0.33	0.12	0.06
$M_{3,3}^f$	0.45	3208	0.33	0.12	0.06
F	0.44	4259	-	0.12	0.13
M_1^i	0.39	2277	3.3	0.01	0.16
M_1^f	0.39	6540, 2907	0	0.01	0.16
M_2^i	0.44	4259	2.62	0.01	0.16
M_2^f	0.44	6814, 4259	0	0.01	0.16
M_3^i	0.44	4259	0	0.12	0.13
$M_{3,1}^f$	0.44	7240, 4685	0	0.12	0.13
$M_{3,3}^f$	0.44	9796, 4259	0	0.12	0.13

case, we observed that the trapped gas column against the fault in the experiment was different than what could be achieved with our previous p_e for models 1-3 (Tab. 4). Because the capillary properties of the C sand in the fault were not directly involved in Experiment A1, we increased p_e in our calibrated models for that specific region ($p_e = 5$ mbar against the lower F sand, and 3.5

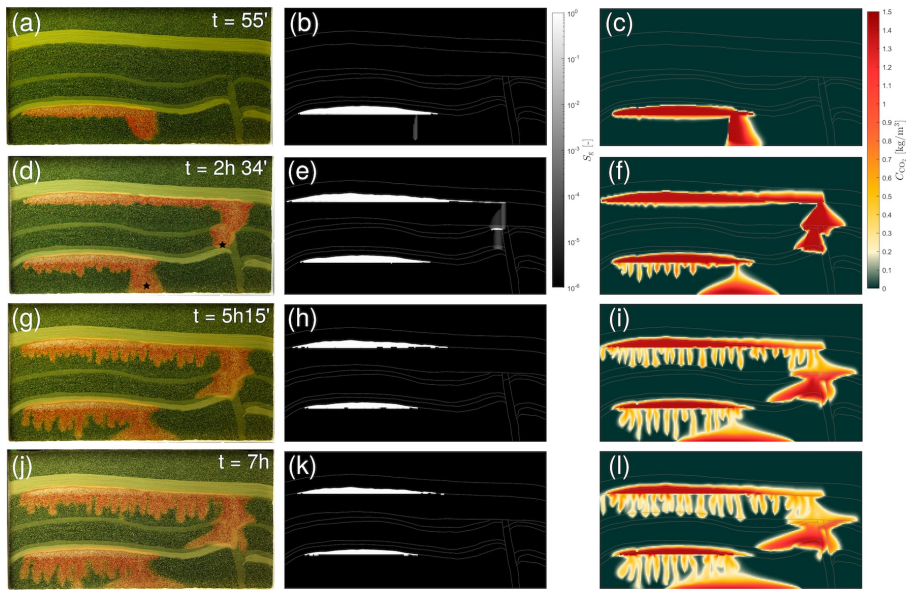


Fig. 12 Comparison between Experiment A1 in Tank 1 (left column) and simulation results with model 3 after calibration (gas saturation shown in middle column, and CO₂ concentration shown in right column). Location of injection ports shown by black stars in **d**. $D = 10^{-9}$ m²/s. **a-c**: End of injection in lower port. **d-f**: End of injection in upper port. **g-i**: Time at which the first finger touches the rig bottom. **j-l**: Time at which the first finger touches the middle C layer.

578 mbar against the middle F sand). All other parameters were taken from the
579 values calibrated to match Experiment A1.

580 Evaluation was performed at the end of injection, at $t = 4$ h 48 min, with
581 a single run with models 1-3. I_R and D were set to the same value in all three
582 models: 1.7 ml/min and 10^{-9} m²/s, respectively. The experimental result is
583 shown in Fig. 13a, while the simulation with model 3 is depicted in Fig. 13b,c.
584 We observe that the general distribution of CO₂ is close to the experimental
585 truth. However, the experiment shows a compact sinking front of the CO₂-rich
586 water without fingers; in our model, gravity fingering is apparent at this stage
587 and fingers are close to the bottom of the rig. Additionally, CO₂-saturated
588 brine touches the right boundary in the upper F reservoir, which does not
589 occur in the experiment. This is due to capillary breach of the C sand above
590 the middle F reservoir, as shown in Fig. 13b, and can be avoided by reducing
591 the gas saturation value at which p_e is defined, or by increasing p_e .

592 The comparison of areal quantities is provided in Fig. 14, and demonstrates
593 good to very good concordance. Model 2 (MAE = 16 cm², CCC = 0.996) and
594 3 (MAE = 14.54 cm², CCC = 0.996) are similarly accurate and slightly better
595 than model 1 (MAE = 20.18 cm², CCC = 0.988), but there are no marked
596 differences.

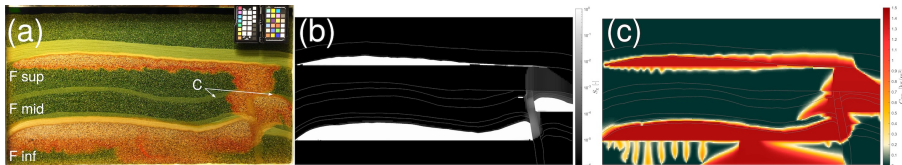


Fig. 13 Comparison between Experiment A2 in Tank 1 (a) and simulation results with model 3 (b,c) at the end of the injection phase ($t = 4\text{h } 48\text{ min}$).

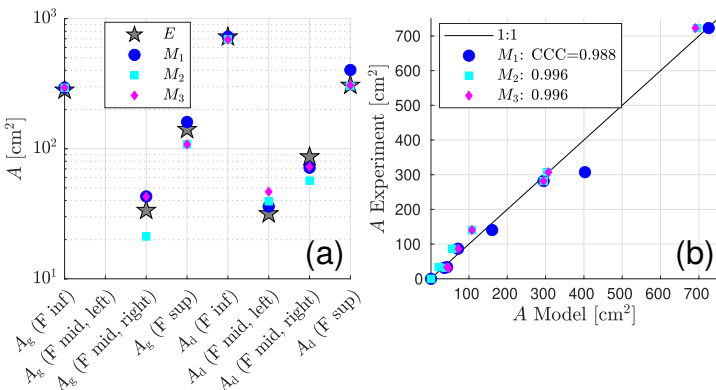


Fig. 14 **a:** Comparison of areas occupied by free gas (A_g) and water with dissolved CO₂ (A_d) for Experiment A2 in Tank 1. Experimental reference shown with a star (E). A_g (F mid, left) not shown because values are very close to 0. Refer to Fig. 6 or Fig. 13a for region location. **b:** Concordance plot for each of the three models, using the same areal quantities as in **a**. Lin's CCC (Lin, 1989) is shown in the key, according to Eq. 2.

4.3.2 Analog for a larger-scale CO₂ injection in a different geologic setting

Finally, we compare the forecasting ability of our calibrated models against Experiment B1, conducted in a larger-scale, more complex geology (Fig. 1e) (Flemisch et al., 2023, this issue). Similar to sect. 4.3.1, our goal is to assess the forecasting ability of our calibrated models—without changing their properties. However, given that sand D controls migration in the lower fault (see Fig. 2e) and it was not present in our calibrated models, we allowed one change for models 1 and 2, which did not have access to local p_c measurements. This means that we ran an initial simulation of this experiment with model 1 and 2, and then adjusted the p_c curve of the D sand. The selected curve lies at $\approx \frac{1}{3}$ of the $p_c(S_w)$ shown in Fig. 3 and Fig. 4, respectively.

Next, we evaluate concordance of models 1–3 by comparing them to the experimental truth after a single run. Evaluation is performed over the total duration of the experiment (120 h), which is simulated with the same I_R (10 ml/min) and D (10^{-9} m²/s) in all three models (M_1 , M_2 , $M_{3,1}$). Additionally, a run with $D = 3 \times 10^{-9}$ m²/s was completed with model 3 ($M_{3,3}$) to better approximate finger widths, as noted in sect. 4.2.

24 *Simulation of geologic CO₂ storage: Value of Local Data and Forecasting*

615 Gas saturation and CO₂ concentration maps at the end of injection with
 616 model 1 are shown in Fig. 15a and Fig. 15b, respectively. The full visual
 617 comparison is provided in Fig. 16. We make the following observations:

- 618 • At the end of injection ($t = 5$ h), all three models forecast some migration
 619 of CO₂ into Box B. Model 2 (Fig. 16c) and 3 (Fig. 16d) underestimate the
 620 amount of CO₂, while model 1 (Fig. 16b) overestimates the amount of CO₂
 621 in the top C sand.
- 622 • Also at the end of injection, all models forecast faster sinking of the CO₂-
 623 charged water tongue arising from the lower injector. This is due to the
 624 higher F sand permeability required to match finger advance (see sect. 4.2),
 625 particularly in model 3 with $D = 3 \times 10^{-9}$ m²/s.
- 626 • The speed at which CO₂-rich fingers sink is slightly faster in our mod-
 627 els, compared to the experiment. As expected, model 3, with a higher
 628 diffusion coefficient, displays thicker fingers, with closer widths to the exper-
 629 iment. Similar to our previous observations, the numerical models cannot
 630 approximate the compact, CO₂-rich water front closely trailing the fingers.
- 631 • Dissolution of CO₂ is underestimated by models 1 and 2, while it is closer,
 632 but overestimated, by model 3.

633 Consistent with our approach described in sect. 3.3, quantitative analysis
 634 is provided by means of areal quantities over time in Fig. 17. Experimental
 635 values were obtained via segmentation of timelapse images, and the data was
 636 reported on a 1×1 cm grid where 0 is pure water, 1 is water with dissolved CO₂,
 637 and 2 is gaseous CO₂. The segmentation procedure is explained in Nordbotten
 638 et al. (2023), this issue. We then obtained the areas of each phase within Box
 639 A and B to generate Fig. 17 (refer to Fig. 15a for box location).

640 In Box A, which contains the main F reservoir and ESF seal, we observe
 641 very good concordance (accurate areas) during injection. Afterwards, model 3
 642 with $D = 3 \times 10^{-9}$ m²/s continues to follow the experiment closely, whereas the
 643 others overestimate gaseous CO₂. Note that the PVT properties of our fluids
 644 are the same in all models; differences arise due to (1) higher sand F S_{wc} in
 645 model 3, and higher sand F k in model 2 and especially model 3 ($D = 3 \times 10^{-9}$
 646 m²/s), compared to model 1, which allow greater convective mixing (Ennis-
 647 King and Paterson, 2005)(Tab. 4); and (2) lower p_e and higher k of sand ESF
 648 in model 2 (Tab. 4), which allows some CO₂ migration into the seal (Fig. 16).
 649 In Box B (Fig. 17d-f), model 1 and model 3 with $D = 10^{-9}$ m²/s are able
 650 to approximately track the experimental truth during injection. However, our
 651 models without dispersion cannot capture the areal increase of CO₂-rich water
 652 that occurs afterwards (cf. Fig. 16).

653 To put these results in perspective, Fig. 18 provides a comparison with
 654 results submitted by the international benchmark study (IBS) participants,
 655 as well as Experiment B1 (Flemisch et al., 2023, this issue). Fig. 18 presents,
 656 for each datapoint, mean Wasserstein distances to experiments and forecasts
 657 (simulations by IBS participants). Specifically, the Wasserstein metric (W)
 658 measures “the minimal effort required to reconfigure the probability mass of

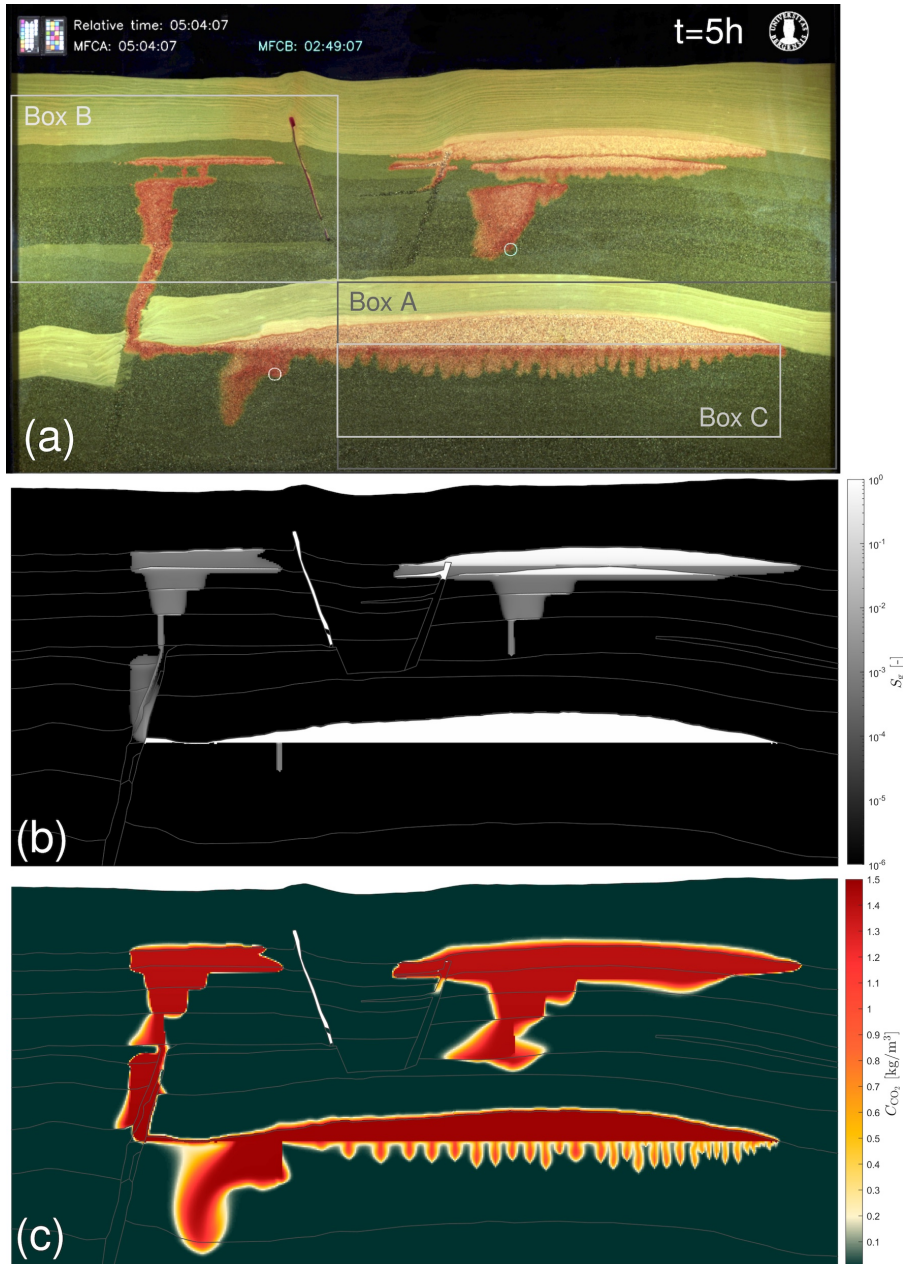


Fig. 15 Comparison between Experiment B1 in Tank 2 (a) and simulation model 1 (b,c) at the end of injection ($t = 5\text{h}$). Circles in a denote the location of injection ports.

one distribution in order to recover the other distribution" (Panaretos and Zemel, 2019). We expect $W \rightarrow 0$ for two samples from the same distribution, given enough values, and two samples to be more similar or concordant the

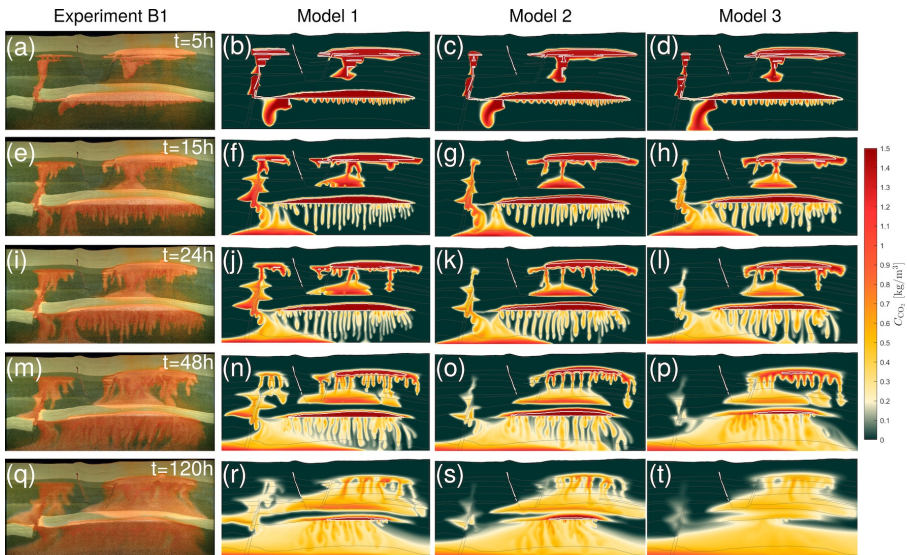


Fig. 16 Comparison between Experiment B1 in Tank 2 (leftmost column) and CO₂ concentration maps for simulation models 1–3 (middle-left, middle-right and rightmost, respectively). $D = 10^{-9} \text{ m}^2/\text{s}$ (model 1 and 2), $D = 3 \times 10^{-9} \text{ m}^2/\text{s}$ (model 3). The white contours in simulation plots indicate $S_g = 10^{-3}$. **a–d** end of injection. **e–h** $t = 15\text{h}$. **i–l** $t = 24\text{h}$. **m–p** $t = 48\text{h}$. **q–t** $t = 120\text{h}$.

closer W is to 0. To calculate distances shown in Fig. 18, the cell mass density in a $1 \times 1 \text{ cm}$ grid was estimated for all simulations and experiments, and then normalized. Therefore, this metric provides a measure of the overall degree of agreement (i.e., in the whole domain). Resulting distances were dimensionalized using the total CO₂ mass in the system, such that the units are grams \times centimeter, with values $< 100 \text{ gr}\cdot\text{cm}$ and $< 50 \text{ gr}\cdot\text{cm}$ representing good concordance and very good concordance, respectively. Details and code are provided by Flemisch et al. (2023, this issue). In Fig. 18, it can be seen that M_1 – M_3 are comparable to or better than the best forecasts by IBS participants. M_1 and $M_{3,1}$, in particular, achieved very good concordance.

Further evaluation of simulation model concordance, including comparison with model results before calibration, mass quantities and error measures, is provided in Appendix A. From this analysis (sect. 4.3 and Appendix A), we find that:

- All matched models approximate well CO₂ migration and distribution in the domain, seal capacity, and onset of convective mixing. M_1 and $M_{3,1}$ are most concordant to experiments (Fig. 18).
- Calibrated models are able to accurately estimate specific quantities during the injection phase, yet they accumulate higher errors later on (Fig. 17 and Appendix A.2).
- Similar to Experiment A1, the calibration procedure significantly improved the concordance of M_1 and M_2 with the experiment (Fig. A1 and Fig. 16). In

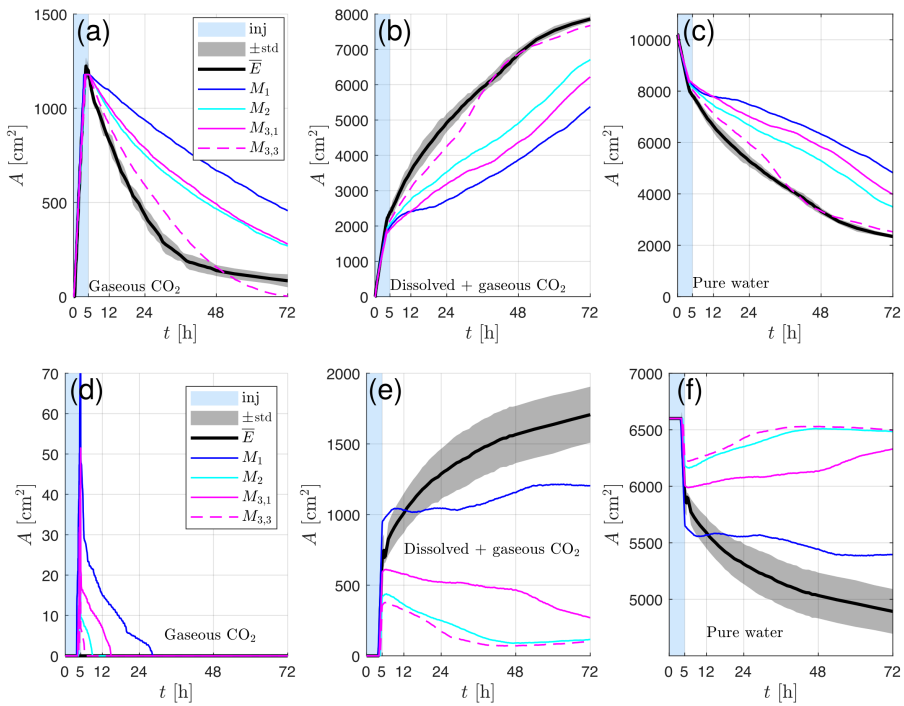


Fig. 17 Comparison of areas occupied by each phase during the first 72h of case B1. Experimental mean (\bar{E}) and standard deviation (std) obtained from four experimental runs with identical protocol, while the results for models 1–3 are for a single run with each matched model. For M_3 , two cases are shown: $D = 10^{-9} \text{ m}^2/\text{s}$ ($M_{3,1}$) and $D = 3 \times 10^{-9} \text{ m}^2/\text{s}$ ($M_{3,3}$). Top row shows areas in Box A, and bottom row shows areas in Box B. **a,d** gaseous CO₂. **b,e** dissolved CO₂ (includes area with gaseous CO₂). **c,f** pure water.

Box A, calibration also improved concordance for M_3 (Fig. A2 and Fig. A6). Overall, however, matched $M_{3,1}$ and $M_{3,3}$ are less concordant than their initial versions, which were already in very good agreement with the experiment (Fig. A3 and Fig. 18).

In summary, calibrated models are transferable to a different operational setting or geologic structure, as long as sediments and trap systems remain the same (Experiment A2 and Box A in Experiment B1). Where reservoir connectivity is provided by heterogeneous structures with uncertain properties, accurate deterministic estimates of CO₂ migration are unlikely; models calibrated elsewhere (Experiment A1) were not accurate in our test (Box B in Experiment B1). Given unlimited computational time, the forecasting capability of numerical models calibrated with published data appears similar to those having access to local measurements; the main value of local data lies in reducing the time required for history matching. Obtained results suggest that history matching worsened M_3 forecasts in a different setting (Experiment B1). Therefore, forecasts in a given geologic setting may benefit more from local measurements and accurate physics, rather than history matching,

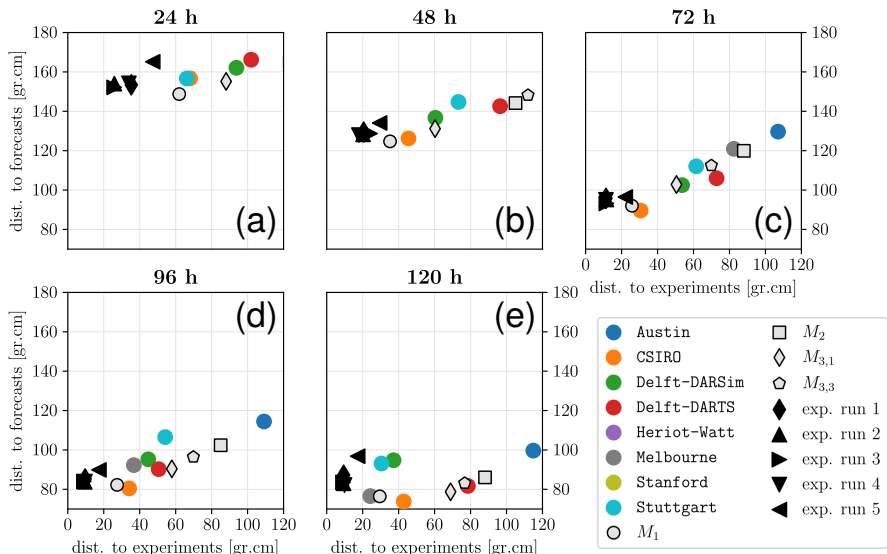


Fig. 18 Wasserstein distances to experiments and forecasts (simulations). Colored circles show forecasts by IBS groups, and results with calibrated models 1–3 are presented with light gray markers. In each subplot, the vertical axis shows the mean distance between a given datapoint and the forecasts (considering the IBS participants only), while the horizontal axis shows the mean distance between a given datapoint and the experiments. Markers not present fall outside of the axes limits. **a:** 24 h. **b:** 48 h. **c:** 72 h. **d:** 96 h. **e:** 120 h.

unless historical data of the same setting is available. This is because CO₂-brine flow is very sensitive to variations in petrophysical properties such as capillary pressure, which will change in different areas, even if the geology is similar.

5 Discussion

In the FluidFlower, strong buoyancy and high permeability lead to persistent appearance and disappearance of fluid phases, as the gas migrates upward and dissolves in the water; coupled with other two-phase flow nonlinearities, these aspects make this problem difficult to solve numerically (e.g., Lie, 2019). Comparison between the number of nonlinear iterations and the strength of different physical mechanisms (flow rates, buoyancy, capillarity and dissolution) are presented in Appendix B. A clear correlation can be seen between flow rates and number of iterations. However, buoyancy, capillarity and dissolution all appear to be playing a role, and it is not straightforward to discern which effect dominates; hence, this is a topic that requires further study. We note that difficulties with the convergence of the nonlinear solver have been reported by all participants in the international benchmark study (Flemisch et al., 2023, this issue). As hinted in sect. 3.1, we addressed this by optimizing linear solver time, reducing the time-step length, increasing the number

720 of time-step cuts and relaxing MRST's maximum normalized residual where
 721 required.

722 In a 2D isotropic medium and assuming uniform flow, the hydrodynamic
 723 dispersion coefficient ($\underline{\underline{D}}_h$) can be modeled as $\underline{\underline{D}}_h = \begin{bmatrix} \alpha_L \bar{u} & 0 \\ 0 & \alpha_T \bar{u} \end{bmatrix}$, where α_L and
 724 α_T are the longitudinal and transverse dispersivity, respectively, and \bar{u} is the
 725 average Darcy velocity (Bear, 1972). Assuming dispersivities $\geq 10^{-3} - 10^{-2}$
 726 m (Garabedian et al., 1991; Gelhar et al., 1992; Schulze-Makuch, 2005) and
 727 $\bar{u} \approx 3 \times 10^{-6}$ m/s (from our simulations), we get $\underline{\underline{D}}_h \in [3 \times 10^{-9}, 3 \times 10^{-8}]$
 728 m²/s or larger; this means that $\underline{\underline{D}}_h \geq D$ for the timescales considered (Riaz
 729 et al., 2004; Rezk et al., 2022). We also note that numerical dispersivity is on
 730 the order of the cell size ($h \approx 4$ mm in Tank 1, and ≈ 5 mm in Tank 2), so
 731 it is likely smaller than hydrodynamic dispersion. Numerical diffusion can be
 732 approximated as uh , which yields maximum values $\sim O(10^{-7}$ m²/s) (water
 733 phase). However, using the mean of the 75th percentile flow velocity over all
 734 time-steps, we obtain $\sim O(10^{-9}$ m²/s). Therefore, we estimate that numerical
 735 diffusion is lower than physical diffusion almost everywhere in our simula-
 736 tions. Previous work suggested that hydrodynamic dispersion in homogeneous
 737 sediments can be accounted for by increasing D (Riaz et al., 2004, 2006), as
 738 done here. However, our analysis shows that the spreading of CO₂-rich water
 739 during convective mixing can be loosely, but not accurately, represented by
 740 molecular diffusion. Given (1) the dominance of convective mixing on solubility
 741 trapping (Ennis-King and Paterson, 2005; Neufeld et al., 2010; MacMinn and
 742 Juanes, 2013); (2) heterogeneity of many natural reservoirs, which increases the
 743 importance of dispersion (Riaz et al., 2006; Bear, 2018); and (3) the accelera-
 744 tion of CO₂ dissolution due to dispersion, as observed here and by others (e.g.,
 745 Hidalgo and Carrera, 2009), it is important to quantify the balance between
 746 diffusion and dispersion to estimate CO₂ trapping.

747 Our study of CO₂ injection and migration in unconsolidated sands at atmo-
 748 spheric p , T conditions captures the CO₂-water system dynamics at short to
 749 intermediate timescales: buoyancy-driven flow and structural trapping (Bachu
 750 et al., 1994; Bryant et al., 2008; Hesse and Woods, 2010; Szulczewski et al.,
 751 2013), residual trapping (Juanes et al., 2006; Burnside and Naylor, 2014) and
 752 convective mixing and dissolution trapping (Weir et al., 1996; Ennis-King and
 753 Paterson, 2005; Riaz et al., 2006; Neufeld et al., 2010; Hidalgo et al., 2012;
 754 MacMinn and Juanes, 2013; Szulczewski et al., 2013). Due to the very large
 755 sand permeability ($10^2 - 10^4$ D), convective mixing and dissolution dominate
 756 CO₂ trapping. With respect to values at ~ 1 km depth ($p \sim 100$ bar, $T \sim 40$
 757 C), the dynamic viscosity and density of CO₂ are $\approx 1/3$ and 3×10^{-3} . Con-
 758 versely, previous studies with similar setups used analogous fluids with density
 759 and viscosity ratios similar to supercritical CO₂-brine (Trevisan et al., 2017;
 760 Krishnamurthy et al., 2022). Dynamics observed in these systems are similar
 761 to ours, with vertical migration of CO₂ dominated by buoyancy and lateral
 762 spreading of CO₂ plumes with a main tongue at the top of the aquifer or high
 763 permeability layer. A quantitative scaling analysis of the FluidFlower (Tank

30 *Simulation of geologic CO₂ storage: Value of Local Data and Forecasting*

2) was performed by Kovscek et al. (2023), who showed that scaling of physical mechanisms to the field scale is possible. Compared to three CO₂ storage projects (Northern Lights, Sleipner and In Salah) the vertical dimension of the storage reservoir is exaggerated 2 to 3 times. Temporally, 1 h in the FluidFlower is equivalent to $\sim 100 - 400$ y in the field; thus, the experiment in Tank 2 (120 h) covers well the injection and post-injection periods. Similar to the FluidFlower, Kovscek et al. (2023) estimate the onset of convective mixing to occur during injection in high-permeability formations like the Utsira Sand (Sleipner). This analysis demonstrates that observations made in the FluidFlower can be used to describe field-scale fluid dynamics and quantify forecasting accuracy.

Our models retained some error at the end of the calibration phase, which is a known problem of manual history matching (Oliver and Chen, 2011). Consistent with previous findings (e.g., Fisher and Jolley, 2007), results show that model 2 and 3, which had access to local data, achieved faster match to the experimental truth than model 1 (sect. 4.2). However, all models seem to have similar forecasting capability (sect. 4.3). Subsurface heterogeneity and time constraints may explain why, in practice, it is critical to include local data to achieve history matching, and, especially, concordant forecasting (e.g., Gosselin et al., 2003; Fisher and Jolley, 2007; Myers et al., 2007; Kam et al., 2015; Avansi et al., 2016). Calibration with Experiment A1 decreased overall concordance of model 3 to Experiment B1 (but improved concordance in Box A), compared to forecasts with initial (measured) parameter values. We interpret this to be the result of fluid migration in Experiment A1 being controlled by different units than in Box B in Experiment B1. Therefore, local measurements are paramount, especially if historical data in the trap system of interest are not available.

Additionally, we did not quantify uncertainty in history-matched models due to the availability of a ground truth. In general, however, this is necessary to manage reservoir operations (e.g., Aanonsen et al., 2009; Oliver and Chen, 2011; Jagalur-Mohan et al., 2018; Jin et al., 2019; Liu and Durlofsky, 2020; Santoso et al., 2021, and references therein). It is also important to note that history-matched models may have grid-size dependencies (see Appendix C), which may require that the grid used to make forecasts, if different or encompassing additional regions, maintain a similar resolution. Finally, multiphase flow in poorly-lithified sediments is non-unique (Haugen et al., 2023, this issue), which also contributes to uncertainty. Therefore, it seems prudent to adopt a probabilistic perspective when estimating subsurface CO₂ migration. This is consistent with results in Fig. 18 and Flemisch et al. (2023, this issue): in the highly-resolved and geologically simple FluidFlower (compared to the subsurface), forecasts by different simulation groups show large spread.

805 6 Conclusions

806 We performed experiments (sect. 2) and numerical simulations (sect. 3) of CO₂
 807 migration in poorly-lithified, siliciclastic sediments at the meter scale. Three
 808 simulation model versions, with access to different levels of local data, were
 809 manually history-matched to the experiments (sect. 4.1, 4.2), and then used
 810 to make forecasts (sect. 4.3). The main findings are:

- 811 1. The time required to history match model 3 (access to both single-phase
 812 and multiphase measurements) is lower than model 2 (access to local single-
 813 phase measurements), which is lower than model 1 (no access to local
 814 petrophysical measurements).
- 815 2. All simulation models achieve a satisfactory qualitative match through-
 816 out the experiments. Quantitatively, forecasting capability of models 1-3
 817 appears similar: in specific domain regions, models were close to the
 818 experimental truth during CO₂ injection, and accumulated larger errors
 819 afterwards, especially where heterogeneous structures control CO₂ migra-
 820 tion.
- 821 3. Overall forecasts with model 3 after calibration in a similar, but not identi-
 822 cal, geologic setting were less accurate than forecasts made with measured
 823 values. This emphasizes the importance of local measurements and history
 824 matching in the same geologic setting.
- 825 4. The addition of a constant molecular diffusion coefficient allows matching
 826 convective finger widths to experimental observations. However, simulations
 827 without dispersion cannot approximate the compact, CO₂-rich sinking front
 828 closely trailing convective fingers in our experiments.

829 Simulation models were not always accurate. Given the degree of control in
 830 our study, it seems prudent to quantify uncertainty when assessing subsurface
 831 CO₂ migration in the field using numerical models. Obtained results suggest
 832 that confidence can be increased by obtaining local data, quantifying petro-
 833 physical parameter uncertainty, testing sensitivity to petrophysical parameters
 834 in different model regions, using historical data from the same setting and
 835 including post-injection data when history matching, and incorporating mul-
 836 tiple scenarios of CO₂ migration, particularly where heterogeneous structures
 837 are at play.

838 **Acknowledgments.** LS gratefully acknowledges laboratory support pro-
 839 vided by UiB Engineer Emil Bang Larsen and image processing support
 840 provided by UiB PhD student Benyamine Benali. LS and RJ are grateful to
 841 Olav Møyner and the MRST team at SINTEF for their guidance to implement
 842 new functionality and continuous support with the MATLAB Reservoir Sim-
 843 ulation Toolbox. A special thanks goes to Robert Gawthorpe, Atle Røtevatn
 844 and Casey Nixon for helpful comments on the geology of North Sea reser-
 845 voirs, which were key to build the geometry in Tank 2, as well as to Bernd
 846 Flemisch for sharing scripts to calculate and visualize Wasserstein distances.

847 The authors thank the three anonymous reviewers for thoughtful and constructive
 848 reviews, which helped improve this manuscript significantly. The authors
 849 also acknowledge support by the following organizations (refer to ‘Funding’
 850 below for details): ExxonMobil, “la Caixa” Foundation, Research Council of
 851 Norway (RCN), Akademia.

852 Statements and Declarations

- 853 • **Funding** This work was supported by ExxonMobil through the project
 854 “Modeling and Mitigation of Induced Seismicity and Fault Leakage during
 855 CO₂ storage”. LS gratefully acknowledges the support of a fellowship
 856 from “la Caixa” Foundation (ID 100010434). The fellowship code is
 857 LCF/BQ/EU21/11890139. MH is funded by the Research Council of Nor-
 858 way (RCN) project no. 280341. KE, MH, JMN and MF are partly funded by
 859 the Centre for Sustainable Subsurface Resources, RCN project no. 331841.
 860 The work of JMN and MF is funded in part through the Akademia project
 861 “FracFlow”.
- 862 • **Competing interests** The authors declare that they have no conflict of
 863 interest.
- 864 • **Availability of data and materials** The dataset for Experiment B1
 865 and data analysis scripts can be obtained from github.com/fluidflower.
 866 The remaining experimental and simulation data are available from the
 867 corresponding authors on reasonable request.
- 868 • **Authors’ contributions** JMN, MF and RJ designed the study and
 869 acquired the funding. JMN, MF and KE conceptualized, designed and built
 870 the FluidFlower rigs. MH, KE and MF conducted the ex-situ sand property
 871 measurements. LS designed the experiments in Tank 1. JMN, MF, MH and
 872 KE designed the experiments in Tank 2. MH, KE, LS and MF conducted
 873 the experiments. LS developed the simulation models and conducted the
 874 simulations. LS, JMN and RJ performed the simulation analysis. LS wrote
 875 the paper, with inputs from all authors.

876 Appendix A Additional analysis of simulation 877 model concordance with 878 Experiment B1

879 A.1 Results with initial model parameters

880 Fig. A1 compares Experiment B1 and concentration maps from simulations
 881 with initial parameters, for each of the three model versions considered. Quali-
 882 tatively, all models estimate the location of the two main gas plumes correctly,
 883 but it is clear that model 1 and 2 are less concordant to the experiment than
 884 model 3. This is particularly true in the upper left of the domain, where CO₂
 885 migration is controlled by the heterogeneous fault. Similar to results presented

in sect. 4.1, model 3 is already very close to the experiment, although the advance of convective fingers is slower.

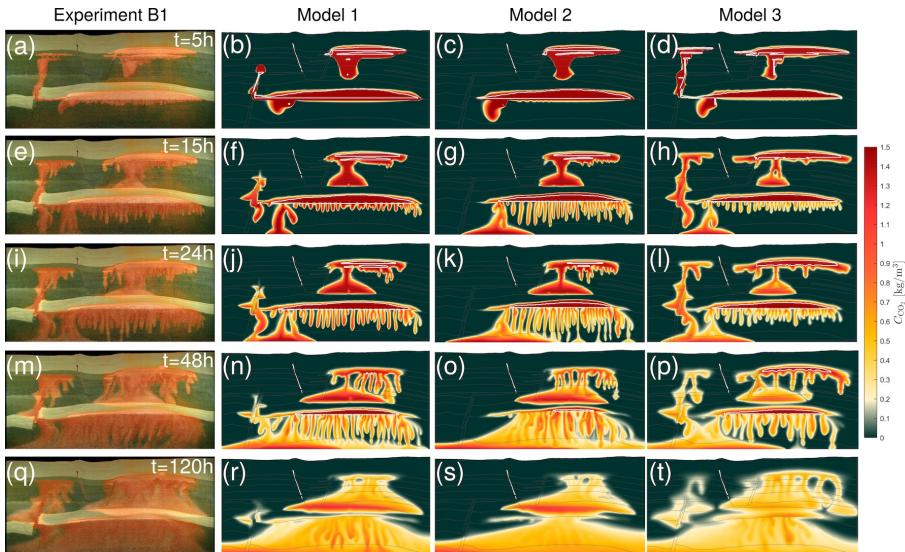


Fig. A1 Comparison between Experiment B1 in Tank 2 (leftmost column) and CO₂ concentration maps for simulation models 1-3 (middle-left, middle-right and rightmost, respectively) with initial parameters. $D = 10^{-9} \text{ m}^2/\text{s}$ (model 1 and 2), $D = 3 \times 10^{-9} \text{ m}^2/\text{s}$ (model 3). **a-d** end of injection. **e-h** $t = 15\text{h}$. **i-l** $t = 24\text{h}$. **m-p** $t = 48\text{h}$. **q-t** $t = 120\text{h}$.

Concordance between our initial models and the simulation is shown in Fig. A2 by means of the ratio between the model and experimental areas for different quantities in Box A and B (see Fig. 15 for box location). Values below 1 indicate that the model underestimates the areal extent of a given quantity, while values above 1 indicate that the model overestimates it. During the first 48–72h, all models except $M_{3,1}$ are reasonably close to the experiment in Box A. Afterwards, M_1 , M_2 and $M_{3,3}$ forecast earlier dissolution of the CO₂ plume, while $M_{3,1}$ forecasts later dissolution. In Box B, concordance is relatively good for M_3 during the first 48h, but model accuracy diminishes with time for all model versions.

Further comparison between our initial model results and experimental values are provided in Fig. A3, where we evaluate mean Wasserstein distances to the international benchmark study (IBS) participants' forecasts and experiments (Flemisch et al., 2023, this issue). Fig. A3 is consistent with Fig. A1, where it can be seen that M_3 is already very close to the experiment, and is similarly concordant or more concordant than the best of the IBS participants.

A.2 Calibrated models

First, we provide the total mass of CO₂ in the computational domain in Fig. A4, and the mass in Boxes A and B in Fig. A5.

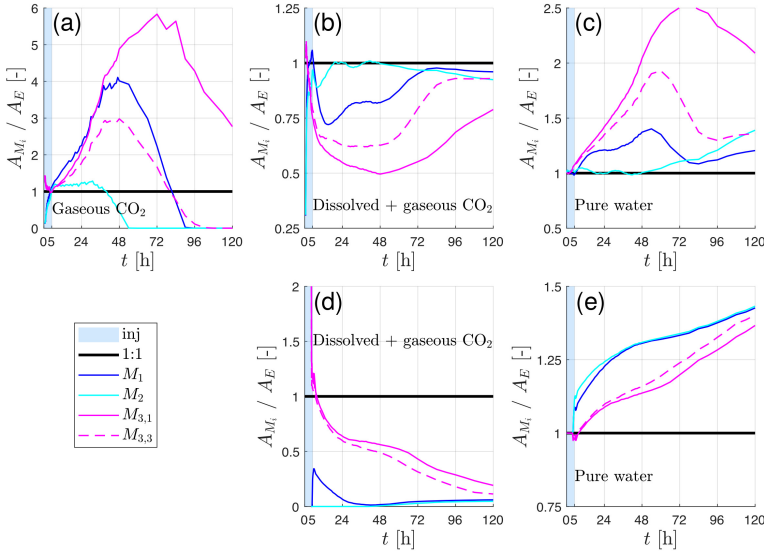


Fig. A2 Ratios between model (A_{M_i}) and experimental mean (A_E) areas occupied by each phase. Experimental mean was obtained from four experimental runs with identical protocol, while the results for models 1–3 are for a single run. For M_3 , two cases are shown: $D = 10^{-9}$ m²/s ($M_{3,1}$) and $D = 3 \times 10^{-9}$ m²/s ($M_{3,3}$). Top row shows Box A, and bottom row shows Box B. Ratios for gaseous CO₂ in Box B are not computed because experimental values are 0. **a** gaseous CO₂. **b,d** dissolved CO₂ (includes area with gaseous CO₂). **c,e** pure water.

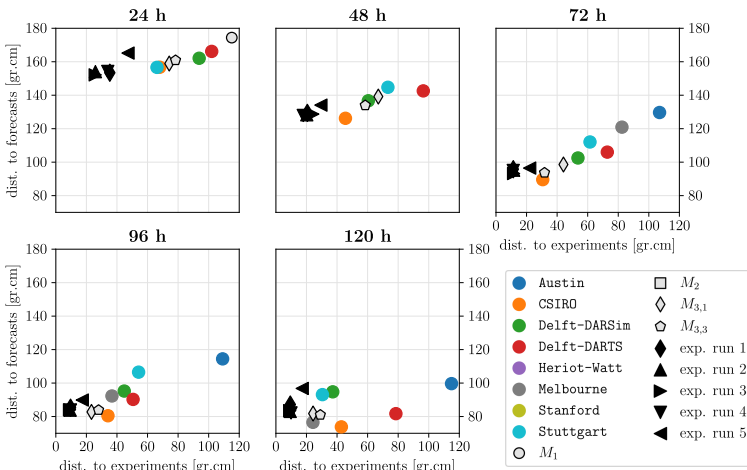


Fig. A3 Wasserstein distances to experiments and forecasts (simulations). Colored circles show forecasts by IBS groups, and results with initial models 1–3 are presented with light gray markers. In each subplot, the vertical axis shows the mean distance between a given datapoint and the forecasts (considering the IBS participants only), while the horizontal axis shows the mean distance between a given datapoint and the experiments. Markers not present fall outside of the axes limits. See sect. 4.3.2 for details.

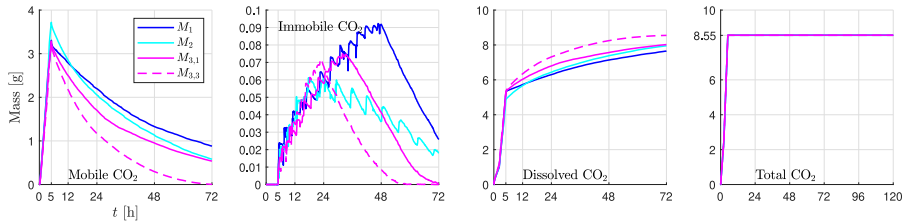


Fig. A4 Total mass of CO₂ for our simulations of Experiment B1 presented in sect. 4.3.2. Results are provided for models 1 to 3. For M_3 , two cases are shown: $D = 10^{-9}$ m²/s ($M_{3,1}$) and $D = 3 \times 10^{-9}$ m²/s ($M_{3,3}$).

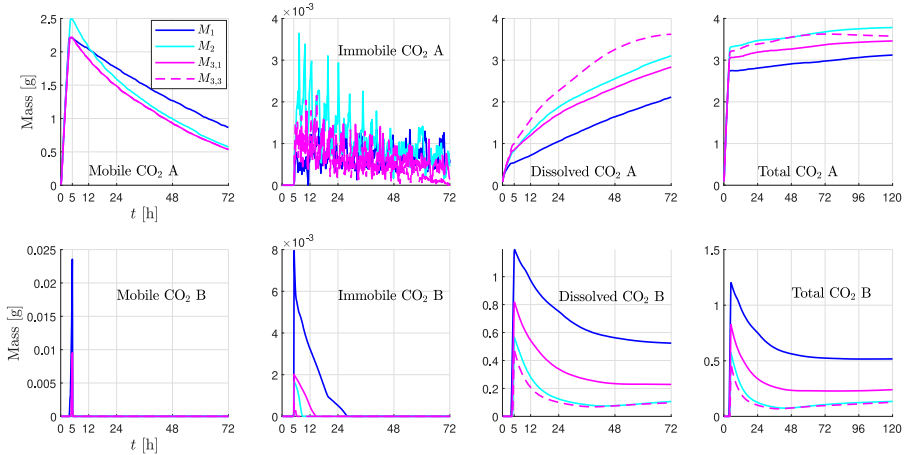


Fig. A5 Mass of CO₂ in Boxes A and B defined in Fig. 1e, for our simulations of Experiment B1 presented in sect. 4.3.2. Results are provided for models 1 to 3. For M_3 , two cases are shown: $D = 10^{-9}$ m²/s ($M_{3,1}$) and $D = 3 \times 10^{-9}$ m²/s ($M_{3,3}$).

907 Next, in Tab. A1, the following measures are compared with quantities
 908 estimated from the experiment via segmentation of timelapse images (Nord-
 909 botten et al., 2023, this issue). These measures correspond to the sparse data
 910 requested to participants of the FluidFlower IBS (Flemisch et al., 2023, this
 911 issue):

- 912 1. time of maximum mobile free phase in Box A
 913 2. mass of mobile CO_{2(g)}, immobile CO_{2(g)}, dissolved CO₂, and CO₂ in the
 914 seal (in any phase), in Box A, 72 h after injection start (2a-d)
 915 3. the same quantities as 2. for Box B (3a-d)
 916 4. time at which m (defined below) exceeds 110% of the width of Box C
 917 5. total mass of CO₂ in the ESF seal, in Box A, at $t = 120$ h

918 Convective mixing in Box C (see Fig. 1e) is reported as the integral of the
 919 magnitude of the gradient in relative concentration of dissolved CO₂ (Flemisch
 920 et al., 2023):

$$m(t) = \int_C \left| \nabla \left(\frac{\chi_{CO_2}^w}{\chi_{CO_2}^{w,max}} \right) \right| d\mathbf{x} \quad (A1)$$

where $\chi_{CO_2}^w$ is the mass fraction of CO₂ in water, and the dissolution limit is $\chi_{CO_2}^{w,max}$. Note that quantity 4, based on m , cannot be provided with full accuracy based on experimental data, so an uncertain lower and upper bound is provided instead. Therefore, error is not computed in Tab. A1.

Relative error is evaluated with respect to the experimental mean (\bar{E}) as $\varepsilon_i(\%) = 100 \times \frac{|\bar{E}_i - M_{J,i}|}{\bar{E}_i}$, where i is a given measure and J refers to any of the models 1-3. In Tab. A1, it can be seen that all models accumulate some error in most of the quantities reported. The maximum errors are $\approx 140\%$ for models 1-2 and $< 100\%$ for model 3. Model 1 is more concordant in the uncertain region (Box B; see sect. 4.3.2 as well), while models 2 and 3 are more accurate in Box A, the region where the calibration performed with Experiment A1 is more meaningful. Overall, $M_{3,1}$ does marginally better.

We provide additional analysis in Fig. A6, which shows ratios between model and experimental areas, similar to Fig. A2. As shown in sect. 4.3.2, $M_{3,3}$ is most concordant in Box A, while M_1 and $M_{3,1}$ do better in Box B. Compared to Fig. A2, the maximum ratio is reduced. In Box A ($t < 72h$), model 1 and 2 are less accurate than in Fig. A2, but this is not representative of their concordance in the whole domain (sect. 4.3.2).

Appendix B Nonlinear solver number of iterations

According to fluid migration in the FluidFlower, flow dynamics are initially dominated by injection rates, then by buoyancy of the gas phase, and finally by capillarity and dissolution. In Fig. B7, we present, for the experiment in Tank 2, the relationship between the number of iterations, the maximum Darcy velocity (u) and the maximum concentration rate (\dot{C}), evaluated as dC/dt , as a function of time. Additionally, we estimated the maximum values of the dimensionless Reynolds (R_e , see Eq. 1), Capillary (C_a) and Bond (B_o) numbers during and after injection (e.g., Bear, 1972):

$$C_a = \frac{\mu_\alpha u_\alpha}{\sigma} \quad (B2)$$

$$B_o = \frac{\Delta \rho g k}{\sigma} \quad (B3)$$

Where μ is the dynamic viscosity, u the Darcy velocity, σ the interfacial tension, $\Delta\rho$ the density difference, g the gravity, k the permeability, and subscript α denotes a generic fluid phase. Max $B_o \sim O(10^{-3})$ and remains constant in our system. Max $C_a \sim O(10^{-6})$, $\sim O(10^{-7})$ for water and $\sim O(10^{-6})$, $\sim O(10^{-8})$ for gas (during and after injection, respectively), while max $R_e \sim O(10^{-2})$ for water and $\sim O(10^{-1})$, $\sim O(10^{-2})$ for gas (during and after injection, respectively).

Table A1 Sparse data comparison between Experiment B1 in Tank 2 and simulation results with models 1-3. Experimental mean and standard deviation were obtained from six experimental runs with identical protocol, while the results for models 1-3 are for a single run with each matched model. For m_3 , two cases are shown: $D = 10^{-9}$ m²/s ($m_{3,1}$) and $D = 3 \times 10^{-9}$ m²/s ($m_{3,3}$). Experimental quantity 4 is reported using a lower and upper bound due to high uncertainty, so errors are not computed. See main text for measure description.

Measure	\bar{E}	$\sigma(E)$	M_1	$\varepsilon_1 [\%]$	M_2	$\varepsilon_2 [\%]$	$M_{3,1}$	$\varepsilon_{3,1} [\%]$	$M_{3,3}$	$\varepsilon_{3,3} [\%]$
1 [s]	14880	720	17700	19	17160	15.3	17280	16.1	18000	21
2a [g]	0.36	0.13	0.87	140.7	0.57	59.7	0.54	48.7	0.005	98.8
2b [g]	0	0	0	0	0	0	0	0	0	0
2c [g]	3.5	0.08	2.11	39.7	3.1	11.3	2.8	19	3.6	3.5
2d [g]	-	-	0.43	n/a	0.97	n/a	0.74	n/a	0.7	n/a
3a [g]	0	0	0	0	0	0	0	0	0	0
3b [g]	0	0	0	0	0	0	0	0	0	0
3c [g]	0.55	0.32	0.52	4.7	0.1	80.7	0.23	58.4	0.1	82.4
3d [g]	n/a	n/a	0.002	n/a	0.006	n/a	0.002	n/a	0.004	n/a
4 [s]	[12180, 17990]	[438, 2261]	15000	n/a	15000	n/a	18600	n/a	15600	n/a
5 [g]	0.38	0.047	0.52	37.1	0.94	148.5	0.73	91.6	0.62	63.1
$\bar{\varepsilon} [\%]$	n/a	n/a	n/a	30.1	n/a	39.4	n/a	29.2	n/a	33.6

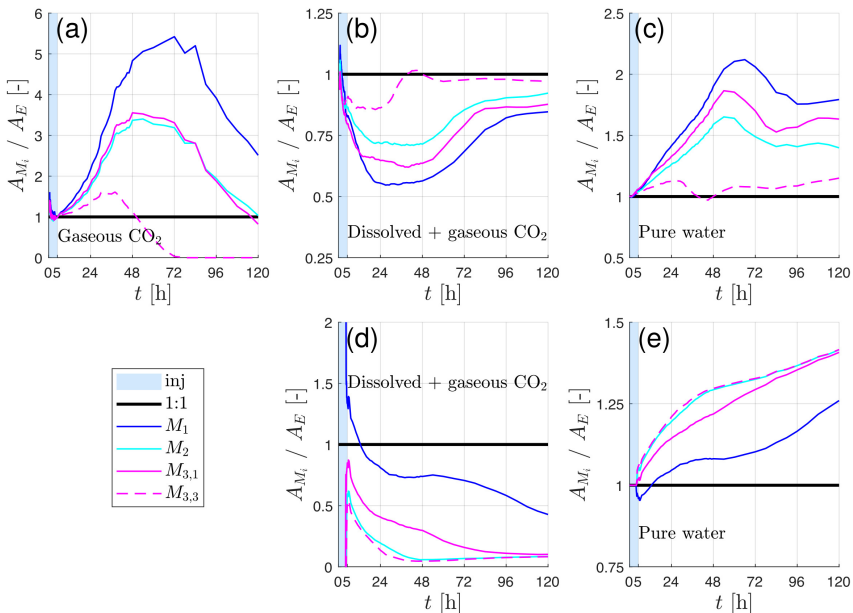


Fig. A6 Ratios between calibrated model (A_{M_i}) and experimental mean (A_E) areas occupied by each phase in case B1. Experimental mean was obtained from four experimental runs with identical protocol, while the results for models 1–3 are for a single run with each model. For M_3 , two cases are shown: $D = 10^{-9}$ m²/s ($M_{3,1}$) and $D = 3 \times 10^{-9}$ m²/s ($M_{3,3}$). Top row shows Box A, and bottom row shows Box B. Ratios for gaseous CO₂ in Box B are not computed because experimental values are 0. **a** gaseous CO₂. **b,d** dissolved CO₂ (includes area with gaseous CO₂). **c,e** pure water.

From Fig. B7, a correlation between $\max |u_{h,g}|$ is apparent during injection. The number of iterations increases significantly after an injection port becomes active, and also when CO₂ spills out of the lower reservoir and starts migrating along the lower fault (see Fig. 15); this occurs at $t \approx 215$ min and $t \approx 250$ for M_1 and $M_{3,3}$, respectively. Peaks in \dot{C} appear at the onset of injection, but we do not observe significant variations otherwise. Values from the dimensionless groups are indicative of high flow rates (R_e close to 1), relatively strong capillary forces, compared to viscous forces ($C_a \sim O(10^{-6})$ or smaller), and appreciable buoyancy. We identify that high flow rates and sudden appearance/disappearance of fluid phases challenge the nonlinear solver during injection. Buoyancy and capillarity forces, which are active throughout the simulation, also impact convergence, but it is not straightforward to identify if one exerts a greater control on the number of iterations. After injection, we observe difficulties between $t \approx 315$ and 1440 min in M_1 , and $t \approx 720$ and 1440 in $M_{3,3}$. Our analysis does not reveal why, so this is a topic that warrants further study.

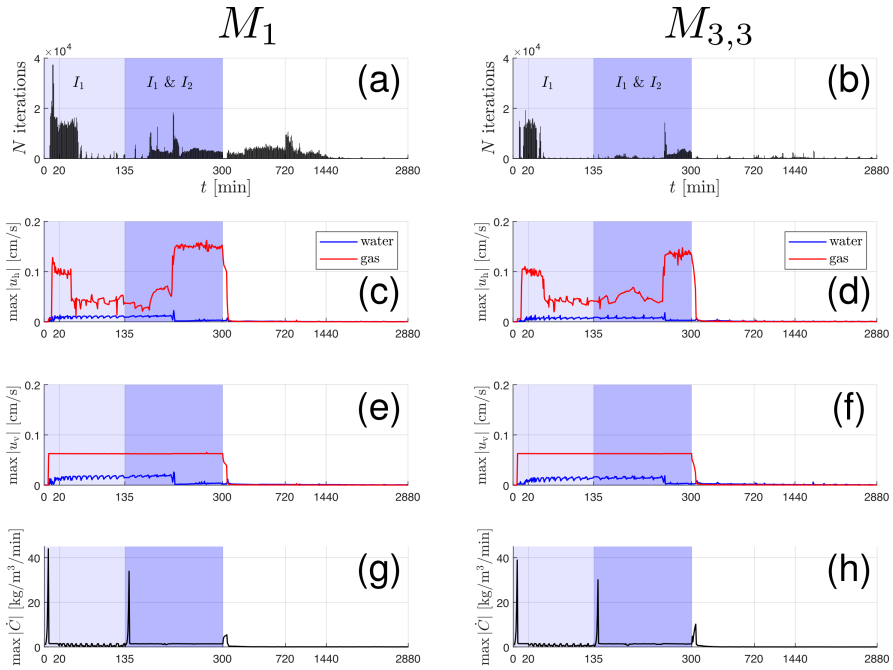


Fig. B7 Number of iterations and maximum values in the simulation domain for various quantities, as a function of time. Results are provided for M_1 (left column) and $M_{3,3}$ (right column). **a,b** Number of nonlinear solver iterations. **c,d** Horizontal Darcy velocity. **e,f** Vertical Darcy velocity. **g,h** Concentration rate (\dot{C}).

Appendix C Comparison of simulation results with multiple grid resolutions

This section provides two comparisons of concentration maps obtained with model 3 after the calibration presented in sect. 4.2:

1. For Experiment A1, we compare two grid sizes: $h = 4$ mm, as shown in the paper, and a coarser grid with $h = 8$ mm (Fig. C8).
2. For Experiment B1, we compare three grid sizes: $h = 5$ mm, used throughout the paper, and two coarser grids with $h = 10$ mm and $h = 20$ mm, respectively (Fig. C9). Note that, in the three simulations in Fig. C9, a total of 8.13 g of CO₂ were injected; this is slightly smaller than the 8.55 g actually injected in the experiment and in our simulations in the rest of the paper.

It can be seen that, for the calibrated parameter set (Tab. 4), the coarser models maintain a general agreement with the finer ones (and the experimental solution). However, some differences are clear even in this qualitative comparison, including (1) smaller extent of the CO₂ plume, (2) lower dissolution, (3) lower number of fingers and finger widths, and (4) different CO₂-rich finger

sinking speed. Therefore, the calibration process is somewhat cell-size dependent, which has implications for applying history matched models from e.g., pilot tests to field-scale CO₂ storage projects.

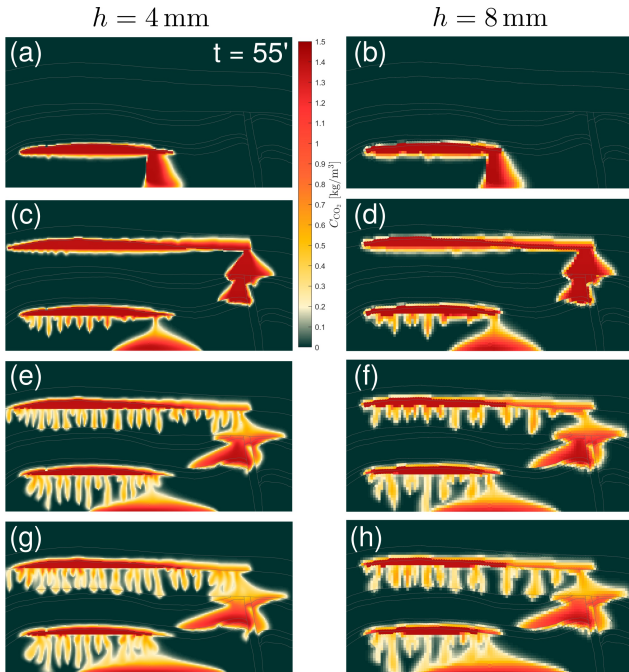


Fig. C8 Concentration maps from our simulations of Experiment A1 with model 3. Results with two grids are shown: $h = 4$ mm (a, c, e, g) and $h = 8$ mm (b, d, f, h).

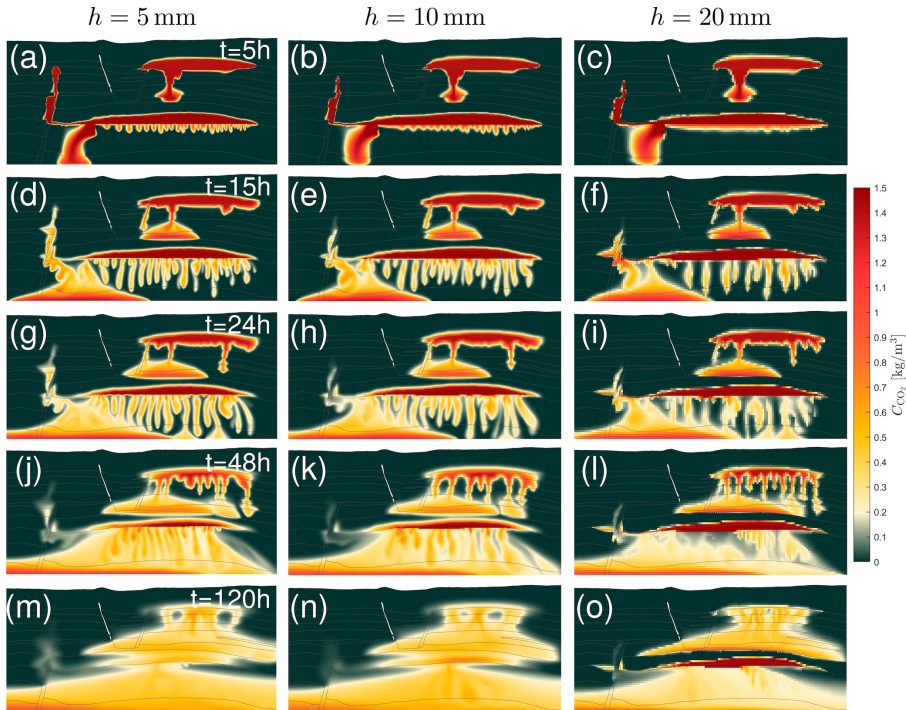


Fig. C9 Concentration maps from simulations of Experiment B1 with model 3. Results with three grids are shown: $h = 5 \text{ mm}$ (a, d, g, j, m), $h = 10 \text{ mm}$ (b, e, h, k, n) and $h = 20 \text{ mm}$ (c, f, i, l, o).

993 References

- 994 Aanonsen, S.I., G. Noevdal, D.S. Oliver, A.C. Reynolds, and B. Vallès. 2009.
 995 The ensemble Kalman filter in reservoir engineering—a review. *SPE
 996 Journal* 14(03): 393–412. <https://doi.org/10.2118/117274-PA>.
- 997 Aissaoui, A. 1983. *Etude théorique et expérimentale de l'hystérisis des pres-
 998 sions capillaires et des perméabilités relatives en vue du stockage souterrain
 999 de gaz*. Ph. D. thesis, Ecole des Mines de Paris, Paris.
- 1000 Alghannam, M. and R. Juanes. 2020. Understanding rate effects in injection-
 1001 induced earthquakes. *Nature Communications* 11(1): 3053. <https://doi.org/10.1038/s41467-020-16860-y>.
- 1003 Askar, A.H., T.H. Illangasekare, and A.M.C. Ilie. 2021. Monitoring brine
 1004 leakage from deep geologic formations storing carbon dioxide: Design frame-
 1005 work validation using intermediate-scale experiment. *Water Resources
 1006 Research* 57(12): e2021WR031005. <https://doi.org/https://doi.org/10.1029/2021WR031005>.
- 1008 Avansi, G.D., C. Maschio, and D.J. Schiozer. 2016. Simultaneous history-
 1009 matching approach by use of reservoir-characterization and reservoir-
 1010 simulation studies. *SPE Reservoir Evaluation & Engineering* 19(04):
 1011 694–712. <https://doi.org/10.2118/179740-PA>.
- 1012 Bachu, S., W. Gunter, and E. Perkins. 1994. Aquifer disposal of CO₂: Hydro-
 1013 dynamic and mineral trapping. *Energy Conversion and Management* 35(4):
 1014 269–279. [https://doi.org/10.1016/0196-8904\(94\)90060-4](https://doi.org/10.1016/0196-8904(94)90060-4).
- 1015 Bear, J. 1972. *Dynamics of Fluids in Porous Media*. Dover. 780 pp.
- 1016 Bear, J. 2018. *Modeling Phenomena of Flow and Transport in Porous Media*,
 1017 Volume 31. Springer. 761 pp.
- 1018 Beard, D. and P. Weyl. 1973. Influence of texture on porosity and permeability
 1019 of unconsolidated sand. *AAPG Bulletin* 57(2): 349–369. <https://doi.org/10.1306/819A4272-16C5-11D7-8645000102C1865D>.
- 1021 Berge, R.L., Ø.S. Klemetsdal, and K.A. Lie. 2019. Unstructured Voronoi grids
 1022 conforming to lower dimensional objects. *Computational Geosciences* 23:
 1023 169–188. <https://doi.org/10.1007/s10596-018-9790-0>.
- 1024 Berge, R.L., Ø.S. Klemetsdal, B. Skaflestad, and K.A. Lie. 2021. The UPR
 1025 module. <https://github.com/rbe051/UPR>.
- 1026 Brock, D. and F. Orr. 1991. Flow visualization of viscous fingering in
 1027 heterogeneous porous media. *SPE Annual Technical Conference and*

- 1028 *Exhibition* (SPE-22614-MS). <https://doi.org/10.2118/22614-MS>.
- 1029 Brooks, R.H. and A.T. Corey 1964. Hydraulic properties of porous media.
1030 Technical report, Colorado State University, Fort Collins, CO.
- 1031 Bryant, S.L., S. Lakshminarasimhan, and G.A. Pope. 2008. Buoyancy-
1032 dominated multiphase flow and its effect on geological sequestration of CO₂.
1033 *SPE Journal* 13(04): 447–454. <https://doi.org/10.2118/99938-PA>.
- 1034 Burnside, N. and M. Naylor. 2014. Review and implications of relative perme-
1035 ability of CO₂/brine systems and residual trapping of CO₂. *International*
1036 *Journal of Greenhouse Gas Control* 23: 1–11. <https://doi.org/10.1016/j.ijggc.2014.01.013>.
- 1038 Caine, J.S., J.P. Evans, and C.B. Forster. 1996. Fault zone architecture and
1039 permeability structure. *Geology* 24(11): 1025–1028. [https://doi.org/10.1130/0091-7613\(1996\)024<1025:FZAAPS>2.3.CO;2](https://doi.org/10.1130/0091-7613(1996)024<1025:FZAAPS>2.3.CO;2).
- 1041 Cappa, F. and J. Rutqvist. 2011. Impact of CO₂ geological sequestration on
1042 the nucleation of earthquakes. *Geophysical Research Letters* 38(17): L17313.
1043 <https://doi.org/10.1029/2011GL048487>.
- 1044 Celia, M.A. 2021. The role of subsurface engineering in the net-zero energy
1045 transition. In *IOP Conference Series: Earth and Environmental Science*,
1046 Volume 861, pp. 072017. IOP Publishing.
- 1047 Childs, C., T. Manzocchi, J.J. Walsh, C.G. Bonson, A. Nicol, and M.P.
1048 Schöpfer. 2009. A geometric model of fault zone and fault rock thick-
1049 ness variations. *Journal of Structural Geology* 31(2): 117–127. <https://doi.org/10.1016/j.jsg.2008.08.009>.
- 1051 Cinar, Y., K. Jessen, R. Berenblyum, R. Juanes, and F.M. Orr. 2006. An
1052 experimental and numerical investigation of crossflow effects in two-phase
1053 displacements. *SPE Journal* 11(02): 216–226. <https://doi.org/10.2118/90568-PA>.
- 1055 Corey, A.T. 1954. The interrelation between gas and oil relative permeabilities.
1056 *Producers Monthly* 19: 38–41.
- 1057 Demidov, D. and R. Rossi. 2018. Subdomain deflation combined with local
1058 AMG: A case study using AMGCL library. *arXiv preprint*. <https://doi.org/10.48550/arXiv.1710.03940>.
- 1060 DiCarlo, D.A., A. Sahni, and M.J. Blunt. 2000. Three-phase relative perme-
1061 ability of water-wet, oil-wet, and mixed-wet sandpacks. *SPE Journal* 5(01):
1062 82–91. <https://doi.org/10.2118/60767-PA>.

44 *Simulation of geologic CO₂ storage: Value of Local Data and Forecasting*

- 1063 Doughty, C. and C.M. Oldenburg. 2020. CO₂ plume evolution in a depleted
 1064 natural gas reservoir: Modeling of conformance uncertainty reduction over
 1065 time. *International Journal of Greenhouse Gas Control* 97: 103026. <https://doi.org/10.1016/j.ijggc.2020.103026>.
- 1067 Duan, Z. and R. Sun. 2003. An improved model calculating CO₂ solubility in
 1068 pure water and aqueous NaCl solutions from 273 to 533 K and from 0 to
 1069 2000 bar. *Chemical Geology* 193(3-4): 257–271. [https://doi.org/10.1016/S0009-2541\(02\)00263-2](https://doi.org/10.1016/S0009-2541(02)00263-2).
- 1071 Eikehaug, K., M. Haugen, O. Folkvord, B. Benali, E.L. Larsen, A. Tinkova,
 1072 A. Røtevatn, J.M. Nordbotten, and M. Fernø. 2023. Engineering meter-scale
 1073 porous media flow experiments for quantitative studies of geological carbon
 1074 sequestration. *Transport in Porous Media* (this issue). Preprint available on
 1075 arXiv through <https://doi.org/10.48550/arXiv.2301.09304>.
- 1076 Ellsworth, W.L. 2013. Injection-induced earthquakes. *Science* 341(6142):
 1077 1225942. <https://doi.org/10.1126/science.1225942>.
- 1078 Ennis-King, J. and L. Paterson. 2005. Role of convective mixing in the
 1079 long-term storage of carbon dioxide in deep saline formations. *SPE
 1080 Journal* 10(03): 349–356. <https://doi.org/10.2118/84344-PA>.
- 1081 European Academies Science Advisory Council (EASAC). Policy Report 35,
 1082 2018. Negative emission technologies: What role in meeting Paris Agree-
 1083 ment targets? https://easac.eu/publications/details/easac_net/. Accessed
 1084 on 01.20.2023.
- 1085 Fernández-García, D., T.H. Illangasekare, and H. Rajaram. 2004. Conservative
 1086 and sorptive forced-gradient and uniform flow tracer tests in a three-
 1087 dimensional laboratory test aquifer. *Water Resources Research* 40(10):
 1088 W10103. <https://doi.org/10.1029/2004WR003112>.
- 1089 Fernø, M., M. Haugen, K. Eikehaug, O. Folkvord, B. Benali, J.W. Both,
 1090 E. Storvik, C.W. Nixon, R.L. Gawthorpe, and J.M. Nordbotten. 2023.
 1091 Room-scale CO₂ injections in a physical reservoir model with faults. *Trans-
 1092 port in Porous Media* (this issue). Preprint available on arXiv through
 1093 <https://doi.org/10.48550/arXiv.2301.06397>.
- 1094 Fisher, Q. and S. Jolley. 2007. Treatment of faults in production simula-
 1095 tion models. *Geological Society, London, Special Publications* 292: 219–233.
 1096 <https://doi.org/10.1144/SP292.13>.
- 1097 Flemisch, B., J.M. Nordbotten, M. Fernø, R. Juanes, H. Class, M. Delshad,
 1098 F. Doster, J. Ennis-King, J. Franc, S. Geiger, D. Gläser, C. Green, J. Gun-
 1099 nning, H. Hajibeygi, S.J. Jackson, M. Jammoul, S. Karra, J. Li, S.K.
 1100 Matthäi, T. Miller, Q. Shao, C. Spurin, P. Stauffer, H. Tchelepi, X. Tian,

- 1101 H. Viswanathan, D. Voskov, Y. Wang, M. Wapperom, M.F. Wheeler,
 1102 A. Wilkins, A.A. Youssef, and Z. Zhang. 2023. The FluidFlower international
 1103 benchmark study: Process, modeling results, and comparison to experimental data.
 1104 *Transport in Porous Media* (this issue). Preprint available on arXiv
 1105 through <https://doi.org/10.48550/arXiv.2302.10986>.
- 1106 Garabedian, S.P., D.R. LeBlanc, L.W. Gelhar, and M.A. Celia. 1991. Large-
 1107 scale natural gradient tracer test in sand and gravel, Cape Cod, Massa-
 1108 chusetts: 2. Analysis of spatial moments for a nonreactive tracer. *Water*
 1109 *Resources Research* 27(5): 911–924. <https://doi.org/10.1029/91WR00242>.
- 1110 Gaucher, D. and D. Lindley. 1960. Waterflood performance in a stratified, five-
 1111 spot reservoir-a scaled-model study. *Transactions of the AIME* 219(01):
 1112 208–215. <https://doi.org/10.2118/1311-G>.
- 1113 Gelhar, L.W., C. Welty, and K.R. Rehfeldt. 1992. A critical review of data on
 1114 field-scale dispersion in aquifers. *Water Resources Research* 28(7): 1955–
 1115 1974. <https://doi.org/10.1029/92WR00607>.
- 1116 Gosselin, O., S. Aanonsen, I. Aavatsmark, A. Cominelli, R. Gonard,
 1117 M. Kolasinski, F. Ferdinandi, L. Kovacic, and K. Neylon. 2003. History
 1118 matching using time-lapse seismic (HUTS). *SPE Annual Technical Confer-
 1119 ence and Exhibition* (SPE 84464). <https://doi.org/10.2118/84464-MS>.
- 1120 Hager, B.H., J. Dieterich, C. Frohlich, R. Juanes, S. Mantica, J.H. Shaw,
 1121 F. Bottazzi, F. Caresani, D. Castineira, A. Cominelli, M. Meda, L. Osculati,
 1122 S. Petroselli, and A. Plesch. 2021. A process-based approach to under-
 1123 standing and managing triggered seismicity. *Nature* 595(7869): 684–689.
 1124 <https://doi.org/10.1038/s41586-021-03668-z>.
- 1125 Hassanzadeh, H., M. Pooladi-Darvish, A.M. Elsharkawy, D.W. Keith, and
 1126 Y. Leonenko. 2008. Predicting PVT data for CO₂–brine mixtures for black-
 1127 oil simulation of CO₂ geological storage. *International Journal of Green-
 1128 house Gas Control* 2(1): 65–77. [https://doi.org/10.1016/S1750-5836\(07\)00010-2](https://doi.org/10.1016/S1750-5836(07)

 1129 00010-2).
- 1130 Haugen, M., L. Saló-Salgado, K. Eikehaug, B. Benali, J.W. Both, E. Storvik,
 1131 O. Folkvord, R. Juanes, J.M. Nordbotten, and M. Fernø. 2023. Physical
 1132 variability in meter-scale laboratory CO₂ injections in faulted geometries.
 1133 *Transport in Porous Media* (this issue). Preprint available on arXiv through
 1134 <https://doi.org/10.48550/arXiv.2301.07347>.
- 1135 Heinemann, Z., C. Brand, M. Munka, and Y. Chen. 1991. Modeling reservoir
 1136 geometry with irregular grids. *SPE Reservoir Engineering* 6(2): 225–232.
 1137 <https://doi.org/10.2118/18412-PA>.

- 1138 Hesse, M. and A. Woods. 2010. Buoyant dispersal of CO₂ during geological
1139 storage. *Geophysical Research Letters* 37(1): L01403. <https://doi.org/10.1029/2009GL041128>.
- 1141 Hidalgo, J.J. and J. Carrera. 2009. Effect of dispersion on the onset of convec-
1142 tion during CO₂ sequestration. *Journal of Fluid Mechanics* 640: 441–452.
1143 <https://doi.org/10.1017/S0022112009991480>.
- 1144 Hidalgo, J.J., J. Fe, L. Cueto-Felgueroso, and R. Juanes. 2012. Scaling of con-
1145 vective mixing in porous media. *Physical Review Letters* 109(26): 264503.
1146 <https://doi.org/10.1103/PhysRevLett.109.264503>.
- 1147 Hommel, J., E. Coltman, and H. Class. 2018. Porosity–permeability relations
1148 for evolving pore space: a review with a focus on (bio-) geochemically altered
1149 porous media. *Transport in Porous Media* 124(2): 589–629. <https://doi.org/10.1007/s11242-018-1086-2>.
- 1151 Ingram, G.M. and J.L. Urai. 1999. Top-seal leakage through faults and frac-
1152 tures: the role of mudrock properties. *Geological Society, London, Special
1153 Publications* 158: 125–135. <https://doi.org/10.1144/GSL.SP.1999.158.01.10>.
- 1154 Intergovernmental Panel on Climate Change (IPCC). 2022. Climate change
1155 2022: Mitigation of climate change, In *Contribution of Working Group III
1156 to the Sixth Assessment Report of the IPCC*, eds. Shukla, P.R., J. Skea,
1157 R. Slade, A. Al Khourdajie, R. van Diemen, D. McCollum, M. Pathak,
1158 S. Some, P. Vyas, R. Fradera, M. Belkacemi, A. Hasija, G. Lisboa, S. Luz,
1159 and J. Malley. Cambridge University Press, Cambridge, UK and New York,
1160 NY, USA. <https://doi.org/10.1017/9781009157926>.
- 1161 Jagalur-Mohan, J., B. Jha, Z. Wang, R. Juanes, and Y. Marzouk. 2018.
1162 Inferring fault frictional and reservoir hydraulic properties from injection-
1163 induced seismicity. *Geophysical Research Letters* 45(3): 1313–1320. <https://doi.org/10.1002/2017GL075925>.
- 1165 Jin, L., H. Lu, and G. Wen. 2019. Fast uncertainty quantification of reservoir
1166 simulation with variational U-Net. *arXiv:1907.00718*. <https://doi.org/10.48550/arXiv.1907.00718>.
- 1168 Juanes, R., B.H. Hager, and H.J. Herzog. 2012. No geologic evidence that
1169 seismicity causes fault leakage that would render large-scale carbon cap-
1170 ture and storage unsuccessful. *Proceedings of the National Academy of
1171 Sciences* 109(52): E3623–E3623. <https://doi.org/10.1073/pnas.1215026109>.
- 1172 Juanes, R., E. Spiteri, F. Orr Jr, and M. Blunt. 2006. Impact of rela-
1173 tive permeability hysteresis on geological CO₂ storage. *Water Resources
1174 Research* 42(12): W12418. <https://doi.org/10.1029/2005WR004806>.

- 1175 Jung, N.H., W.S. Han, Z. Watson, J.P. Graham, and K.Y. Kim. 2014. Fault-
1176 controlled CO₂ leakage from natural reservoirs in the Colorado Plateau,
1177 East-Central Utah. *Earth and Planetary Science Letters* 403: 358–367.
1178 <https://doi.org/10.1016/j.epsl.2014.07.012>.
- 1179 Kam, P., M. Nadeem, A. Novlesky, A. Kumar, and E.N. Omatsone. 2015.
1180 Reservoir characterization and history matching of the Horn River shale:
1181 an integrated geoscience and reservoir-simulation approach. *Journal of*
1182 *Canadian Petroleum Technology* 54(06): 475–488. <https://doi.org/10.2118/171611-PA>.
- 1184 Killough, J.E. 1976. Reservoir simulation with history-dependent saturation
1185 functions. *SPE Journal* 16(01): 37–48. <https://doi.org/10.2118/5106-PA>.
- 1186 Kneafsey, T.J. and K. Pruess. 2010. Laboratory flow experiments for visual-
1187 izing carbon dioxide-induced, density-driven brine convection. *Transport in*
1188 *Porous Media* 82: 123–139. <https://doi.org/10.1007/s11242-009-9482-2>.
- 1189 Kovscek, A.R., J.M. Nordbotten, and M.A. Ferno. 2023. Scaling up Fluid-
1190 Flower results for carbon dioxide storage in geological media. *Transport*
1191 *in Porous Media* (this issue). Preprint available on arXiv through <https://doi.org/10.48550/arXiv.2301.09853>.
- 1193 Krishnamurthy, P.G., D. DiCarlo, and T. Meckel. 2022. Geologic hetero-
1194 geneity controls on trapping and migration of CO₂. *Geophysical Research*
1195 *Letters* 49(16): e2022GL099104. <https://doi.org/10.1029/2022GL099104>.
- 1196 Krishnamurthy, P.G., T.A. Meckel, and D. DiCarlo. 2019. Mimicking geo-
1197 logic depositional fabrics for multiphase flow experiments. *Water Resources*
1198 *Research* 55(11): 9623–9638. <https://doi.org/10.1029/2019WR025664>.
- 1199 Krogstad, S., K. Lie, O. Møyner, H.M. Nilsen, X. Raynaud, and B. Skaflestad.
1200 2015. MRST-AD – an open-source framework for rapid prototyping and
1201 evaluation of reservoir simulation problems. *SPE Reservoir Simulation*
1202 *Conference*: 1–20. <https://doi.org/SPE-173317-MS>.
- 1203 Land, C.S. 1968. Calculation of imbibition relative permeability for two-
1204 and three-phase flow from rock properties. *Society of Petroleum Engineers*
1205 *Journal* 8(02): 149–156. <https://doi.org/10.2118/1942-PA>.
- 1206 Landa-Marbán, D., T.H. Sandve, J.W. Both, J.M. Nordbotten, and S.E.
1207 Gasda. 2023. Performance of an open-source image-based history matching
1208 framework for CO₂ storage. Forhtcoming.
- 1209 Lassen, R.N., M.R. Plamper, T. Sakaki, T.H. Illangasekare, J. Gudbjerg, T.O.
1210 Sonnenborg, and K.H. Jensen. 2015. Effects of geologic heterogeneity on
1211 migration of gaseous CO₂ using laboratory and modeling investigations.

- 1212 1213 International Journal of Greenhouse Gas Control 43: 213–224. <https://doi.org/10.1016/j.ijggc.2015.10.015>.
- 1214 1215 1216 1217 Lenhard, R., M. Oostrom, C. Simmons, and M. White. 1995. Investigation
of density-dependent gas advection of trichloroethylene: Experiment and a
model validation exercise. *Journal of Contaminant Hydrology* 19(1): 47–67.
[https://doi.org/10.1016/0169-7722\(94\)00055-M](https://doi.org/10.1016/0169-7722(94)00055-M).
- 1218 1219 Leverett, M.C. 1941. Capillary behavior in porous solids. *Transactions of the
AIME* 142(01): 152–169. <https://doi.org/10.2118/941152-G>.
- 1220 1221 1222 Lie, K.A. 2019. *An Introduction to Reservoir Simulation Using MATLAB/GNU Octave: User Guide for the MATLAB Reservoir Simulation
Toolbox (MRST)*. Cambridge, UK: Cambridge University Press.
- 1223 1224 Lie, K.A. and O. Møyner eds. 2021. *Advanced Modeling with the MATLAB
Reservoir Simulation Toolbox*. Cambridge, UK: Cambridge University Press.
- 1225 1226 Lin, L.I.K. 1989. A concordance correlation coefficient to evaluate reproducibil-
ity. *Biometrics*: 255–268. <https://doi.org/10.2307/2532051>.
- 1227 1228 1229 Liu, Y. and L.J. Durlofsky. 2020. Multilevel strategies and geological
parameterizations for history matching complex reservoir models. *SPE
Journal* 25(01): 081–104. <https://doi.org/10.2118/193895-PA>.
- 1230 1231 1232 MacMinn, C.W. and R. Juanes. 2013. Buoyant currents arrested by convective
dissolution. *Geophysical Research Letters* 40(10): 2017–2022. <https://doi.org/10.1002/grl.50473>.
- 1233 1234 1235 1236 Marcucci, A., S. Kypreos, and E. Panos. 2017. The road to achieving
the long-term Paris targets: energy transition and the role of direct air
capture. *Climatic Change* 144 (2): 181–193. <https://doi.org/10.1007/s10584-017-2051-8>.
- 1237 1238 1239 1240 Myers, R.D., A. Allgood, A. Hjellbakk, P. Vrolijk, and N. Briedis. 2007. Test-
ing fault transmissibility predictions in a structurally dominated reservoir:
Ringhorne Field, Norway. *Geological Society, London, Special Publica-
tions* 292(1): 271–294. <https://doi.org/10.1144/SP292.16>.
- 1241 1242 1243 1244 Neufeld, J.A., M.A. Hesse, A. Riaz, M.A. Hallworth, H.A. Tchelepi, and
H.E. Huppert. 2010. Convective dissolution of carbon dioxide in saline
aquifers. *Geophysical Research Letters* 37(22): L22404. <https://doi.org/10.1029/2010GL044728>.
- 1245 1246 1247 Ni, H., S. Bakhshian, and T. Meckel. 2023. Effects of grain size and small-
scale bedform architecture on CO₂ saturation from buoyancy-driven flow.
Scientific Reports 13: 2474. <https://doi.org/10.1038/s41598-023-29360-y>.

- 1248 Nordbotten, J.M., B. Benali, J.W. Both, B. Brattekås, E. Storvik, and
1249 M. Fernø. 2023. DarSIA: An open-source python toolbox for two-scale
1250 image processing for porous media. *Transport in Porous Media* (this issue).
1251 Preprint available on arXiv through <https://doi.org/10.48550/arXiv.2301.05455>.
- 1253 Nordbotten, J.M. and M.A. Celia. 2012. *Geological Storage of CO₂: Modeling*
1254 *Approaches for Large-scale Simulation*. Hoboken, New Jersey: Wiley. 242
1255 pp.
- 1256 Nordbotten, J.M., M. Fernø, B. Flemisch, R. Juanes, and M. Jørgensen. 2022.
1257 *Final Benchmark Description: FluidFlower International Benchmark Study*.
1258 <https://doi.org/10.5281/zenodo.6807102>.
- 1259 Nordbotten, J.M., B. Flemisch, S.E. Gasda, H. Nilsen, Y. Fan, G.E. Pickup,
1260 B. Wiese, M.A. Celia, H.K. Dahle, G.T. Eigestad, and K. Pruess. 2012.
1261 Uncertainties in practical simulation of CO₂ storage. *International Journal*
1262 *of Greenhouse Gas Control* 9: 234–242. <https://doi.org/10.1016/j.ijggc.2012.03.007>.
- 1264 Oldenburg, C.M. 2018. Are we all in concordance with the meaning of the word
1265 conformance, and is our definition in conformity with standard definitions?
1266 *Greenhouse Gases: Science and Technology* 8(2): 210–214. <https://doi.org/10.1002/ghg.1773>.
- 1268 Oliver, D.S. and Y. Chen. 2011. Recent progress on reservoir history matching:
1269 a review. *Computational Geosciences* 15(1): 185–221. <https://doi.org/10.1007/s10596-010-9194-2>.
- 1271 Panaretos, V.M. and Y. Zemel. 2019. Statistical aspects of Wasserstein
1272 distances. *Annual Review of Statistics and Its Application* 6: 405–431.
1273 <https://doi.org/10.1146/annurev-statistics-030718-104938>.
- 1274 Pentland, C.H., E. Itsekiri, S.K. Al Mansoori, S. Iglauder, B. Bijeljic, and M.J.
1275 Blunt. 2010. Measurement of nonwetting-phase trapping in sandpacks. *SPE*
1276 *Journal* 15(02): 274–281. <https://doi.org/10.2118/115697-PA>.
- 1277 Plug, W.J. and J. Bruining. 2007. Capillary pressure for the sand–CO₂–water
1278 system under various pressure conditions. application to CO₂ sequestration.
1279 *Advances in Water Resources* 30(11): 2339–2353. <https://doi.org/10.1016/j.advwatres.2007.05.010>.
- 1281 Rezk, M.G., J. Foroozesh, A. Abdulrahman, and J. Gholinezhad. 2022. CO₂
1282 diffusion and dispersion in porous media: Review of advances in experimental
1283 measurements and mathematical models. *Energy & Fuels* 36(1): 133–155.
1284 <https://doi.org/10.1021/acs.energyfuels.1c03552>.

50 *Simulation of geologic CO₂ storage: Value of Local Data and Forecasting*

- 1285 Riaz, A., M. Hesse, H. Tchelepi, and F. Orr. 2006. Onset of convection in a
1286 gravitationally unstable diffusive boundary layer in porous media. *Journal of*
1287 *Fluid Mechanics* 548: 87–111. <https://doi.org/10.1017/S0022112005007494>.
- 1288 Riaz, A., C. Pankiewitz, and E. Meiburg. 2004. Linear stability of radial
1289 displacements in porous media: influence of velocity-induced dispersion and
1290 concentration-dependent diffusion. *Physics of Fluids* 16(10): 3592–3598.
1291 <https://doi.org/10.1063/1.1775431>.
- 1292 Saadatpoor, E., S.L. Bryant, and K. Sepehrnoori. 2010. New trapping mech-
1293 anism in carbon sequestration. *Transport in Porous Media* 82(1): 3–17.
1294 <https://doi.org/10.1007/s11242-009-9446-6>.
- 1295 Saló-Salgado, L., J.S. Davis, and R. Juanes. 2023. Fault permeability from
1296 stochastic modeling of clay smears. *Geology* 51(1): 91–95. <https://doi.org/10.1130/G50739.1>.
- 1298 Saló-Salgado, L., O. Møyner, K.A. Lie, and R. Juanes. 2023. Three-
1299 dimensional simulation of geologic carbon sequestration using MRST-ad-
1300 blackoil. Forthcoming.
- 1301 Santoso, R.K., X. He, M. Alsinan, H. Kwak, and H. Hoteit. 2021. Bayesian
1302 long-short term memory for history matching in reservoir simulations. *SPE*
1303 *Reservoir Simulation Conference* (SPE-203976-MS). <https://doi.org/10.2118/203976-MS>.
- 1305 Schlumberger 2014. *ECLIPSE Technical description* (2014.1 ed.). Schlum-
1306 berger Ltd.
- 1307 Schulz, R., N. Ray, S. Zech, A. Rupp, and P. Knabner. 2019. Beyond Kozeny–
1308 Carman: predicting the permeability in porous media. *Transport in Porous*
1309 *Media* 130(2): 487–512. <https://doi.org/10.1007/s11242-019-01321-y>.
- 1310 Schulze-Makuch, D. 2005. Longitudinal dispersivity data and implications for
1311 scaling behavior. *Groundwater* 43(3): 443–456. <https://doi.org/10.1111/j.1745-6584.2005.0051.x>.
- 1313 Silliman, S. and E. Simpson. 1987. Laboratory evidence of the scale effect
1314 in dispersion of solutes in porous media. *Water Resources Research* 23(8):
1315 1667–1673. <https://doi.org/10.1029/WR023i008p01667>.
- 1316 Smits, K.M., T. Sakaki, A. Limsuwat, and T.H. Illangasekare. 2010. Thermal
1317 conductivity of sands under varying moisture and porosity in drainage–
1318 wetting cycles. *Vadose Zone Journal* 9(1): 172–180. <https://doi.org/10.2136/vzj2009.0095>.

- 1320 Spiteri, E.J., R. Juanes, M.J. Blunt, and F.M. Orr. 2008. A new model of trapping
1321 and relative permeability hysteresis for all wettability characteristics.
1322 *SPE Journal* 13(03): 277–288. <https://doi.org/10.2118/96448-PA>.
- 1323 Spycher, N. and K. Pruess. 2005. CO₂-H₂O mixtures in the geological sequestration of CO₂. II. Partitioning in chloride brines at 12–100 C and up to
1324 600 bar. *Geochimica et Cosmochimica Acta* 69(13): 3309–3320. <https://doi.org/10.1016/j.gca.2005.01.015>.
- 1325 1326 Spycher, N., K. Pruess, and J. Ennis-King. 2003. CO₂-H₂O mixtures in the geological sequestration of CO₂. I. Assessment and calculation of mutual
1327 solubilities from 12 to 100 C and up to 600 bar. *Geochimica et Cosmochimica Acta* 67(16): 3015–3031. [https://doi.org/10.1016/S0016-7037\(03\)00273-4](https://doi.org/10.1016/S0016-7037(03)00273-4).
- 1328 1329 Szulczewski, M., M. Hesse, and R. Juanes. 2013. Carbon dioxide dissolution in structural and stratigraphic traps. *Journal of Fluid Mechanics* 736: 287–315.
1330 <https://doi.org/10.1017/jfm.2013.511>.
- 1331 1332 Timur, A. 1968. An investigation of permeability, porosity, & residual water saturation relationships for sandstone reservoirs. *The Log Analyst* 9(04):
1333 8–17.
- 1334 1335 Trevisan, L., A. Cihan, F. Fagerlund, E. Agartan, H. Mori, J.T. Birkholzer,
1336 Q. Zhou, and T.H. Illangasekare. 2014. Investigation of mechanisms of supercritical CO₂ trapping in deep saline reservoirs using surrogate fluids at ambient laboratory conditions. *International Journal of Greenhouse Gas Control* 29: 35–49. <https://doi.org/10.1016/j.ijggc.2014.07.012>.
- 1342 1343 Trevisan, L., R. Pini, A. Cihan, J.T. Birkholzer, Q. Zhou, A. González-Nicolás,
1344 and T.H. Illangasekare. 2017. Imaging and quantification of spreading and trapping of carbon dioxide in saline aquifers using meter-scale laboratory experiments. *Water Resources Research* 53(1): 485–502. <https://doi.org/10.1002/2016WR019749>.
- 1345 1346 Verdon, J.P., J.M. Kendall, A.L. Stork, R.A. Chadwick, D.J. White, and R.C. Bissell. 2013. Comparison of geomechanical deformation induced by megatonne-scale CO₂ storage at Sleipner, Weyburn, and In Salah. *Proceedings of the National Academy of Sciences* 110(30): E2762–E2771. <https://doi.org/10.1073/pnas.1302156110>.
- 1352 1353 Vilarrasa, V. and J. Carrera. 2015. Geologic carbon storage is unlikely to trigger large earthquakes and reactivate faults through which CO₂ could leak. *Proceedings of the National Academy of Sciences* 112(19): 5938–5943.
1354 <https://doi.org/10.1073/pnas.1413284112>.
- 1356 1357 Wang, S., M. Lee, M.K. Park, and J.M. Kim. 2010. Box experiments on monitoring the CO₂ migration in a homogeneous medium using electrical

52 *Simulation of geologic CO₂ storage: Value of Local Data and Forecasting*

- 1358 resistivity survey. *Geosciences Journal* 14: 77–85. <https://doi.org/10.1007/s12303-010-0009-1>.
- 1360 Weir, G.J., S.P. White, and W.M. Kissling. 1996. Reservoir storage and
1361 containment of greenhouse gases. *Transport in Porous Media* 23: 37–60.
1362 <https://doi.org/10.1007/BF00145265>.
- 1363 Wood, B.D., C.N. Dawson, J.E. Szecsody, and G.P. Streile. 1994. Modeling
1364 contaminant transport and biodegradation in a layered porous media sys-
1365 tem. *Water resources research* 30(6): 1833–1845. <https://doi.org/10.1029/94WR00434>.
- 1366
- 1367 Zoback, M.D. and S.M. Gorelick. 2012. Earthquake triggering and large-scale
1368 geologic storage of carbon dioxide. *Proceedings of the National Academy of
1369 Sciences* 109(26): 10164–10168. <https://doi.org/10.1073/pnas.1202473109>.